Dependence of the upward terrestrial radiance within the (3.5–4.0) μm spectral range on thermodynamic and composition parameters of the atmosphere(*)

C. Tomasi, V. Vitale, R. Ricci, A. Lupi and A. Cacciari

ISAC-CNR - Via Gobetti 101, 40129 Bologna, Italy

Summary. — Calculations of the upward infrared radiance reaching outer space within the (3.5–4.0) μm wavelength range were carried out to define the dependence features of the signals measured by radiometers onboard satellites on the temperature, moisture and composition parameters of the atmosphere. In particular, simulations of upwelling radiance were performed for application to the measurements taken by the AVHRR radiometers mounted aboard the NOAA-7 to NOAA-16 satellites and the SEVIRI instrument mounted aboard the Second Generation Meteosat (MSG-1) satellite launched in 2002. The calculations were made using a modified version of computer code LOWTRAN 7 for a large set of atmospheric vertical profiles of temperature and humidity parameters, each one represented with a set of 324 isothermal layers from sea-level to 100 km height and derived from one of 23 atmospheric models relative to different latitudes and seasons. For all these atmospheric configurations, we determined the temperature deficit ΔT, as given by the difference between the surface temperature and apparent emission temperature of the surface, the latter quantity being obtained in terms of black-body emission theory from the satellite measurement of upward radiance. Parameter ΔT was found to depend mainly on the total atmospheric content of water vapour and the shape of the vertical profile of temperature within the ground layer: it was found to vary considerably passing from cases of marked thermal inversions to cases of adiabatic or superadiabatic temperature gradients. Considering sets of atmospheric models where precipitable water was assumed to remain constant, ΔT was found to decrease appreciably as the temperature gradient increases from negative values (in the presence of thermal inversions) to positive ones (for adiabatic and superadiabatic lapse rates at the ground), presenting negative slopes that become gradually more marked as the ground layer depth increases.

Considering sets of atmospheric models where the moisture parameters were assumed to vary widely, ΔT was found to change linearly as a function of precipitable water, with slope coefficients varying slowly from positive to negative values, as the temperature gradient increases from negative to positive values. As a consequence of these dependence features, the ratio between ΔT and precipitable water was found to increase as a function of surface temperature, following patterns closely best-fitted by second-order polynomial curves. Dependence features of ΔT on the mean atmospheric concentrations of methane and nitrous oxide were also determined. Similarly, ΔT was found to vary linearly as a function of aerosol optical thickness in the visible for polydispersions of maritime, rural, urban and tropospheric aerosols, presenting the most marked slope in the case of maritime aerosols. An overall procedure is proposed for calculating ΔT, taking into account i) the latitudinal and seasonal conditions of the atmosphere, ii) estimates of ground-level temperature and precipitable water, as derived from satellite and/or ground-based measurements of meteorological parameters, iii) aerosol optical thickness at visible wavelengths, and iv) CH_4 and N_2O atmospheric concentrations.

PACS `92.60.Fm` – Boundary layer structure and processes.
PACS `92.60.Jq` – Water in the atmosphere (humidity, clouds, evaporation, precipitation).
PACS `92.60.Ta` – Interaction of atmosphere with electromagnetic waves; propagation.
PACS `42.68.-w` – Atmospheric optics.

1. – Introduction

The atmospheric transmittance spectrum measured within the visible and infrared wavelength range shows several intervals characterised by high transparency features, situated between various strong absorption bands of water vapour, carbon dioxide and ozone. Among these highly transparent regions, which are commonly called "atmospheric windows", the wavelength interval from 3.5 to 4.0 μm generally exhibits the highest transmittance features among those appearing throughout the atmospheric spectrum from 0.25 to 30 μm and beyond. This window is limited on the left side by the group of vibro-rotational bands ν_3, ν_1 and $2\nu_2$ due to water vapour (corresponding to the main fundamental transitions at the 2.663, 2.734 and 3.173 μm wavelengths), and on the right side by the vibro-rotational bands ν_3 and $(\nu_1 + \nu_2)$ of the carbon dioxide molecule, which correspond to the main fundamental transitions at 4.257 and 4.815 μm wavelengths, respectively [1].

Numerous measurements of upward terrestrial radiance have been performed over the past years, and they are now routinely taken within this spectral interval by the AVHRR radiometers mounted aboard the NOAA satellites in order to measure the radiation fluxes reaching the outer atmospheric boundaries, such observational data being of great benefit for both climatological and meteorological studies. The various AVHRR radiometers mounted aboard the operational sun-synchronous satellites NOAA-7 to NOAA-14 and NOAA-16 have provided and continue to provide measurements of the radiance emitted by the Earth-atmosphere system towards space in the 3.55–3.93 μm wavelength interval [2-4]. Upward radiance measurements in this spectral range are also currently taken in scientific experiments performed with the SEVIRI instrument mounted aboard the

MSG-1 satellite [5, 6].

These satellite measurements of upward terrestrial radiance can be analysed very usefully in order to determine with good precision the emission temperature of the sea surface (SST) and, more generally, of the terrestrial surface, provided that atmospheric transmission and emission models are appropriately used for different latitudinal and seasonal conditions. The comparison between the measurements taken within the 3.5–4.0 μm radiometric channel and those furnished by the same radiometers in other infrared channels [7-11] can also provide useful information on the thermal features of the Earth surface. Upward radiance measurements from satellites at different infrared channels can also be used in order to obtain cloud classification diagrams, as well as reliable evaluations of the cloud-top temperature [12, 13].

Mainly because of water vapour, minor gases and aerosol particles, the atmosphere attenuates to a not negligible extent the thermal radiation emitted upward by the surface within the wavelength range from 3.5 to 4.0 μm. Thus, only a limited fraction of the radiation emitted by the surface reaches outer space. Moreover, the radiation emitted upward by the various atmospheric layers (which are generally colder than the terrestrial surface) turns out to be considerably attenuated by the overlying atmosphere. As a consequence of such concurring emission, absorption and scattering processes, the terrestrial radiance reaching space is generally smaller than the radiance emitted directly by the Earth's surface. In other words, the temperature value T_b calculated as the equivalent temperature that corresponds—in terms of the black-body emission theory—to the upward radiance measurement provided by a satellite radiometer is generally smaller than the real surface emission temperature T_s. The difference

$$\Delta T = T_s - T_b \tag{1}$$

is commonly called "temperature deficit". This quantity assumes positive values in the most real cases [9].

The above remarks suggest very strongly that the temperature deficit produced by the atmospheric attenuation processes is only partly compensated by atmospheric emission contributions. Thus, ΔT is expected to be related very closely to the total contents and the vertical distribution features of the atmospheric constituents that absorb and/or scatter the infrared radiation. In the 3.5–4.0 μm spectral range, several atmospheric gases cause intense absorption, while aerosol particles can produce marked scattering effects in particular cases characterised by high values of the aerosol optical thickness, such as those presenting layers of haze droplets near the ground [14]. Therefore, before evaluating how extensively the temperature deficit ΔT relative to the 3.5–4.0 μm spectral interval varies as a function of the meteorological and atmospheric composition parameters, it seems useful to describe the most significant spectral features of the atmospheric extinction processes occurring within this spectral range.

2. – Atmospheric extinction features in the 3.5–4.0 μm wavelength range

The infrared radiation attenuation in the 3.5–4.0 μm atmospheric window is mainly due to i) selective absorption by water vapour (due to both H_2O and HDO molecules), ii) selective absorption by methane (CH_4), nitrous oxide (N_2O) and other minor gases, iii) continuum absorption by both water vapour and nitrogen (N_2), and iv) aerosol extinction. The spectral features of these attenuation processes are as follows:
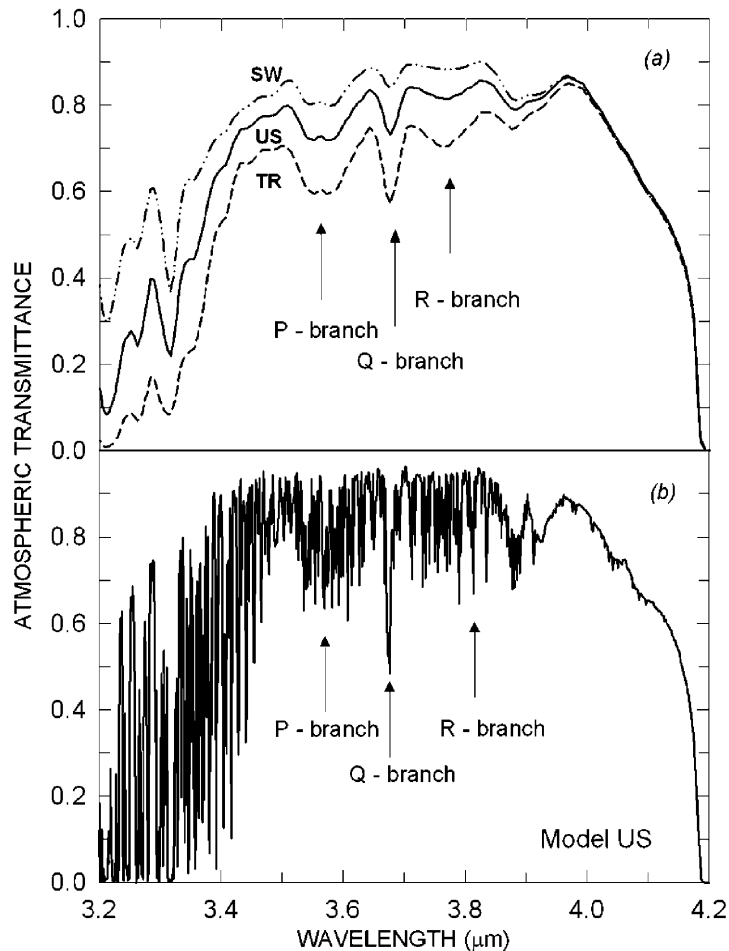
Fig. 1. – a) Spectral curves of atmospheric transmittance determined in the 3.2–4.2 μm wavelength range using the computer code LOWTRAN 7 [16] for the atmospheric models called Subarctic Winter (SW), US Standard Atmosphere 1976 (US) and Tropical (TR) [17, 18]. Aerosol particle extinction was calculated in terms of the rural aerosol particle extinction model [19] normalised to visual range $V_0 = 23$ km at ground level. b) Spectral curves of atmospheric transmittance obtained using the computer code MODTRAN 4 [20, 21] for the atmospheric model US [17, 18]. The arrows indicate the spectral features associated with the three branches P, Q, and R of the HDO band.

1) *Selective absorption by water vapour*: it is mainly produced by isolated lines in the right wing of the absorption band $2\nu_2$, which is often labelled with the Greek letter X′ [15]. As shown in fig. 1, the atmospheric attenuation spectrum in this wavelength range is dominated by the presence of the strong vibro-rotational absorption band ν_1, produced by HDO molecules, which consists of the typical Q-branch centred at wavelength $\lambda = 3.672$ μm and of the side-branches P and R covering the whole spectral range from 3.478 to 3.922 μm [22]. In reality, the HDO molecular concentration in the atmosphere is very low, commonly evaluated to be equal to about 3×10^{-4} times the H_2O molecule

concentration [23, 24]. Nevertheless, the intensities of the HDO absorption lines are generally so strong as to yield very high values of the partial atmospheric optical thickness associated with the selective water vapour absorption in the 3.5–4.0 μm spectral window, as can be seen in fig. 2. Due to the strong intensity characteristics of the HDO lines, the spectral features of this band can also be easily recognised in the emission spectra of atmospheric radiance measured from ground-level stations [25].

2) *Selective absorption by other gases*: it is mainly due to the molecules of methane (CH$_4$) and nitrous oxide (N$_2$O). The strong vibro-rotational band ν_3 of methane has its fundamental transition at 3.312 μm wavelength. Other two vibro-rotational bands of CH$_4$ are the ($\nu_2 + \nu_4$) and 2ν_4 bands, which are centred at 3.542 and 3.846 μm wavelengths, respectively, presenting several strong absorption lines within the 3.5–4.0 μm atmospheric window. In particular, the right wing of the ν_3 band exhibits important absorption features at wavelengths shorter than 3.65 μm, as can be seen in figs. 1 and 2. The nitrous oxide absorption spectrum presents a weak absorption band centred at 3.574 μm and three other more intense absorption bands corresponding to transitions located at 3.881, 3.901 and 4.063 μm wavelengths [1]. Figure 2 shows that the absorption caused by these strong bands yields optical thickness values varying between 10^{-2} and 10^{-1} in the 3.85–3.97 μm wavelength interval. Another thirteen weak bands due to various isotopic forms of the N$_2$O molecule are present throughout the 3.574–4.041 μm spectral range [26].

Numerous weak absorption lines are also produced by the carbon dioxide (CO$_2$) molecule, due to i) nine weak absorption bands, distributed through the wavelength range from 3.5 to 4.0 μm, and ii) six other bands from 4.057 to 4.140 μm. The extinction effects produced by this long sequence of weak absorption bands overlap to the wing effects caused by the nearby strong absorption band of CO$_2$, centred at $\lambda = 4.257$ μm and by the not far bands of water vapour and nitrous oxide in the range $\lambda > 4.225$ μm.

The ozone (O$_3$) molecule exhibits a weak absorption band centred at the 3.590 μm wavelength. Other weak absorption bands are due to the molecules of formaldehyde (five bands centred at wavelengths ranging from 3.517 to 4.000 μm), sulphur dioxide (one band centred at $\lambda = 4.000$ μm), nitrogen dioxide (one band centred at $\lambda = 3.441$ μm), hydrogen bromide (two bands, both centred at about $\lambda = 3.908$ μm) and hydrogen chloride (two bands centred at 3.465 and 3.468 μm, respectively), as well as by OH radicals (four bands centred at 3.430, 3.634, 3.868 and 4.141 μm wavelengths). All these absorption bands were examined by means of laboratory measurements and spectroscopic studies [26-28] to define their spectral absorption features with appropriate values of the shape-parameters of their absorption lines. However, the O$_3$ band and all the above-mentioned bands of the other gases are very weak, and cause in practice only negligible effects on the upwelling infrared radiance measured from satellites.

3) *Continuum absorption by water vapour and nitrogen*: it yields spectral features that can be easily recognised in the atmospheric transmittance spectrum shown in fig. 1. The atmospheric water vapour continuum was represented by Kneizys *et al.* [16] as the sum of the two following terms [29]:

a) a foreign-broadening term, which is attributed to the spectral broadening of the absorption lines produced by collisions between air and water molecules and, according to the collision-broadening theory, is proportional to the dry air pressure through a coefficient depending closely on air temperature [30]; and

b) a self-broadening term, which is attributed to the spectral broadening of the absorption lines caused by mutual collisions between water molecules and is directly propor-
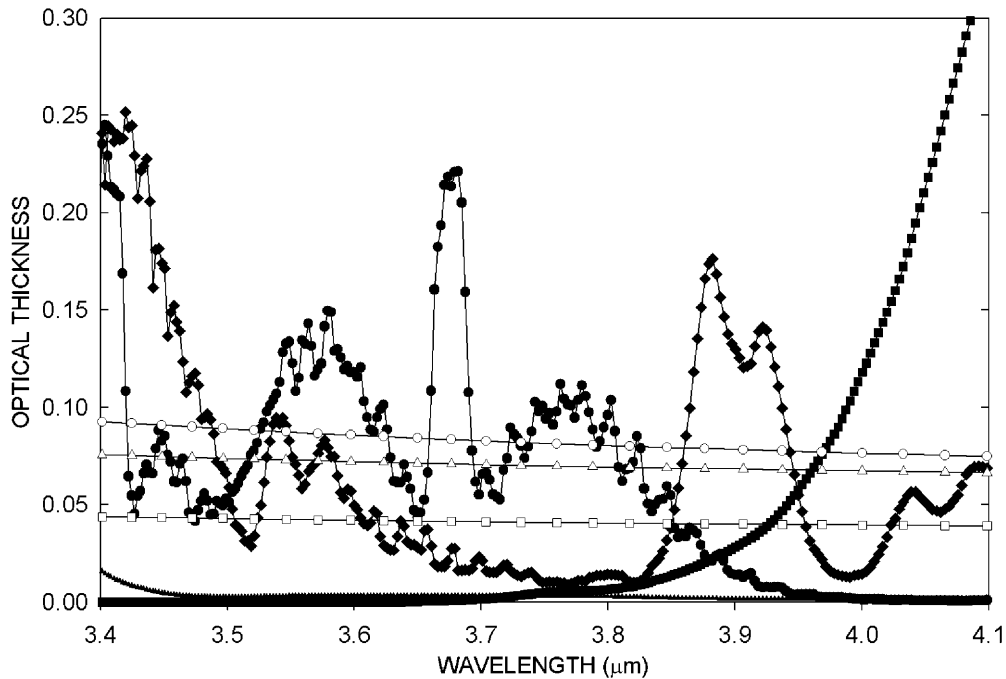
Fig. 2. – Spectral curves of the partial optical depths produced in the US Standard Atmosphere 1976 (model US) [16-18] by 1) water vapour selective absorption, due to H_2O and HDO molecules (solid circles), 2) water vapour continuum (solid triangles), 3) nitrogen continuum (solid squares), 4) minor gases, such as methane, nitrous oxide, carbon dioxide and ozone, considered all together (solid diamonds), 5) the rural aerosol particle model [19], normalised to visual range $V_0 = 15$ km at ground level (open squares), 6) the maritime aerosol particle model [19], normalised to $V_0 = 23$ km (open circles), and 7) the urban aerosol particle model [19], normalised to $V_0 = 12$ km (open triangles).

tional to the water vapour partial pressure through a coefficient that sharply decreases as a function of increasing air temperature [30].

The spectral curve of the partial optical thickness given by the overlapping of the two water vapour continuum components is shown in fig. 2, as obtained for the atmospheric model commonly called US Standard Atmosphere 1976 (model US) [16-18]. As can be seen, the optical thickness due to the overall water vapour continuum turns out to be considerably smaller than that produced by the selective water vapour absorption.

The nitrogen molecule presents intense continuum absorption features beyond the 3.9 μm wavelength, which are described with good accuracy by Kneizys *et al.* [31]. This continuum is associated with a dipole moment induced by collisions in the homopolar molecule of nitrogen. Figure 2 shows the spectral dependence curve of the optical thickness produced by this pressure-induced absorption of the N_2 molecules in the 3.5–4.0 μm spectral range, for standard conditions of the atmosphere (model US) [16-18].

4) *Atmospheric extinction by aerosol particles*: as predicted by the Mie theory, airborne aerosol particles extinguish infrared radiation by both scattering and absorption. The spectral features of these attenuation effects depend on several parameters, mainly the shape of the columnar aerosol size-distribution curve, the vertical profile of total par-

ticle number concentration, the spectral characteristics of both real and imaginary parts of the particulate matter refractive index, and the shape-parameters of aerosol particles, which are known not to have usually spherical shapes. It is also important to point out that both the shape of the aerosol size-distribution curve and the complex refractive index of particulate matter are closely related to the origin, formation and evolution processes of the aerosol particles and, hence, depend also on the relative humidity conditions of the air masses where the aerosols are suspended [32]. It is difficult to define realistic aerosol extinction models, since the shape of the particle size-distribution curve usually varies with time and is very often characterised by multimodal features covering the particle size range from a few tens of Ångströms to some tens of micrometers. This is true not only of industrial sites but also ones very distant from urban areas [33]. When the relative humidity of air increases, aerosol particles begin to grow by condensation and the number density concentrations of both accumulation and coarse particles tend to increase [34]. Consequently, such particles may play an increasing role in extinguishing the infrared radiation [35]. As shown by Volz [36], the real part of the particulate matter refractive index can present greatly differing values in the 3.5–4.0 μm spectral interval, depending on the physico-chemical properties of the aerosol particles: values ranging from 1.1 to more than 1.3 are frequently found in soot particles, while values varying from 1.2 to 1.6 are typical of water soluble substances and sea-salt particles. Correspondingly, the imaginary part of the refractive index assumes values of about 10^{-3} for sea-salt particle polydispersions, about 10^{-2} for water soluble substances and between 0.1 and 1.0 for soot particles [36, 37].

The large variability of the dielectric properties of particulate matter clearly implies that the absorption produced by aerosol particles within the 3.5–4.0 μm atmospheric window can change considerably from one case to another. In order to give an idea of the variability of the aerosol extinction characteristics as a function of number density, size-distribution curve parameters and particulate refractive index, fig. 2 shows the spectral curves of the particulate optical thickness $\tau_a(\lambda)$, as calculated for various aerosol extinction models presenting particle polydispersions of diverse origins [19] and different values of the visual range V_0 at ground level. These results indicate that the infrared radiation extinction due to large columnar contents of aerosol particles can sometimes be so intense as to cause a strong attenuation of the radiation emitted upward by the terrestrial surface and, consequently, yield very high values of temperature deficit ΔT in this spectral window. Thus, the upward radiance emitted by the surface-atmosphere system is expected to depend not only on the temperature conditions and water vapour content of the atmosphere, but also on the columnar atmospheric content and radiative characteristics of aerosol particles.

3. – The atmospheric models

The spectral distribution functions of atmospheric transmission relative to aerosol particles, Rayleigh scattering and atmospheric gases can be calculated with the spectral resolution of 5 cm^{-1} by means of the computer sub-routines [19, 26-28] employed in the computer codes LOWTRAN 7 and MODTRAN 4 [16, 20, 21, 31]. Calculations of both downward and upward radiation fluxes through the atmosphere can be obtained for different thermodynamic conditions of the atmosphere, which are usually described by means of atmospheric models defined for various latitudes and seasonal conditions. The spectral attenuation and emission characteristics of the atmosphere can be accurately calculated using partial transmittance sub-routines, which enable us to determine

TABLE I. – *Values of surface temperature T_0, absolute humidity q_0 at sea level, precipitable water w and temperature gradient γ for the 23 atmospheric models [17, 39-41] chosen for the present calculations of upwelling radiance in the 3.5–4.0 μm spectral range.*

Model number	Atmospheric model	T_0 (K)	q_0 (g m^{-3})	w (g cm^{-2})	γ (K/km)
1	Tropical (TR)	300.0	19.0	4.12	−6.0
2	Mid-latitude Winter (MW)	272.2	3.5	0.85	−3.5
3	Mid-latitude Summer (MS)	294.0	14.0	2.92	−4.0
4	Subarctic Winter (SW)	257.1	1.2	0.42	+ 2.0
5	Subarctic Summer (SS)	287.0	9.1	2.09	−5.0
6	U. S. Standard 1976 (US)	288.1	5.9	1.42	−6.5
7	Milan Winter	276.2	5.4	0.95	+ 1.8
8	Milan Spring	296.2	13.4	2.07	−12.5
9	Milan Summer	303.2	16.7	2.60	−17.4
10	Milan Autumn	288.2	9.6	1.27	−10.0
11	Po Valley Winter (00:00 GMT)	276.3	5.0	0.95	+ 6.9
12	Po Valley Winter (12:00 GMT)	278.5	5.1	0.82	−0.8
13	Po Valley Spring (00:00 GMT)	288.4	9.5	1.65	−1.5
14	Po Valley Spring (12:00 GMT)	293.5	10.1	1.55	−12.7
15	Po Valley Summer (00:00 GMT)	296.2	14.5	2.73	+ 1.5
16	Po Valley Summer (12:00 GMT)	301.5	15.0	2.26	−13.5
17	Po Valley Autumn (00:00 GMT)	281.3	7.6	1.28	+ 5.6
18	Po Valley Autumn (12:00 GMT)	286.5	7.9	1.20	−7.1
19	Alpex Spring (00:00 GMT)	280.7	6.0	1.15	+ 5.8
20	Alpex Spring (06:00 GMT)	279.4	6.0	1.10	+ 8.2
21	Alpex Spring (12:00 GMT)	287.1	6.9	1.02	−8.3
22	Alpex Spring (18:00 GMT)	285.4	5.5	1.02	−2.1
23	Indian Ocean (IO)	300.6	22.4	5.11	−7.3

the spectral curves of the partial transmission terms through the various atmospheric layers, relative to Rayleigh scattering, molecular absorption and aerosol scattering and absorption, separately.

For the present study, the twenty-three atmospheric models listed in table I were used. Each atmospheric model is characterised by a mean vertical profile of temperature and a mean vertical curve of absolute humidity, corresponding to a certain season, latitude and area of the planet. The first six models in table I are those presented by McClatchey *et al.* [17]. The other four models, hereinafter called the Milan models, are those defined by Tomasi [38] through the analysis of radiosounding data taken at the Milan Linate Airport station (Italy) at 13:00 local time (12:00 GMT) during various seasons. The eight Po Valley models are those determined by Tomasi and Paccagnella [39] from radiosoundings taken at the Milan Linate Airport station (Italy) during different seasonal periods in various years, considering separately the nocturnal and diurnal conditions of the atmospheric boundary layer, since they are strongly diversified as a result of the intense processes of solar heating or nocturnal cooling at the ground. Another four models, called Alpex Spring models, were defined by Tomasi and Paccagnella [39] from radiosounding measurements taken during the Alpex measurement campaign in spring 1982, at four different times (00:00 GMT, 06:00 GMT 12:00 GMT and 18:00 GMT) of the day and at three radiosounding stations in the Po Valley area. The last model

was determined by Tomasi [40] from a large set of meteorological data taken with forty radiosoundings performed in an equatorial area of the Indian Ocean, not far from the Seychelles Islands. For all the above 23 models, the vertical distribution curves of air temperature, absolute humidity and other meteorological parameters (dew-point, relative humidity, water vapour partial pressure, air total pressure) were determined by Tomasi and Deserti [41] at 208 significant levels from the surface to 100 km height, through the following procedure:

i) in each model, the temperature was assumed to vary linearly as a function of altitude, from one significant level to the subsequent one;

ii) in each model, the absolute humidity was assumed to vary exponentially as a function of altitude from each significant level to the subsequent one;

iii) in the altitude range from 12 to 100 km, the four Milan models were assumed to present similar vertical profiles of temperature and moisture parameters to those given by the Mid-latitude models [17];

iv) the eight Po Valley models [39], defined only in the altitude range from the surface to 10 km, were assumed to present the vertical distribution curves of temperature and moisture parameters determined by Tomasi and Deserti [41] at upper levels from 10 to 100 km, in close agreement with those of the Mid-latitude models [17];

v) the four Alpex Spring models [39], defined in the height range from the surface to 25 km, were assumed to present the vertical curves of temperature and moisture parameters calculated by Tomasi and Deserti [41] in the altitude range from 25 to 100 km;

vi) the Indian Ocean model [40], defined in the altitude range from the sea surface to 24 km, was assumed to have the same vertical distribution curves of temperature and moisture parameters given by the Tropical model [17] from 30 to 100 km height, while the vertical profiles of temperature and humidity parameters from 24 to 30 km were determined according to the interpolation criteria described at points i) and ii), respectively.

On the basis of these assumptions, the values of temperature and absolute humidity were calculated at levels varying in steps of i) 25 m through the altitude range from 0 to 1 km, ii) 50 m from 1 to 2 km, iii) 100 m from 2 to 5 km, iv) 200 m from 5 to 12 km, v) 250 m from 12 to 20 km, vi) 500 m from 20 to 30 km, vii) 1 km from 30 to 50 km, and viii) 5 km from 50 to 100 km. For all the 23 atmospheric models in table I, the values of air pressure, air temperature, moisture parameters and water vapour content in the vertical column of unit cross-section from the sea-level to altitude z were assumed to be those calculated by Tomasi and Deserti [41] at 208 fixed values of z ranging from 0 to 100 km. The values of atmospheric precipitable water w are also listed in table I, as given by the sum of the partial columnar contents of water vapour mass within the 207 atmospheric layers defined by the above-fixed levels.

For all the 23 atmospheric models, we also calculated the values of the temperature gradient γ from the surface to 0.4 km height given in the last column of table I. Since strong processes of surface cooling or heating can occur within the ground layer of the atmosphere, parameter γ gives a measure of the vertical stability or instability conditions characterising the lower part of the boundary layer in each model. Examining the results in table I, it can be seen that the vertical profile of temperature exhibits:

1) marked inversions and, hence, absolute stability conditions of the ground layer in the Subarctic Winter, Milan Winter and Po Valley Winter (00:00 GMT) models;

2) well-defined stability features throughout the ground layer in the US Standard Atmosphere 1962, Subarctic Summer and Indian Ocean models; and

3) absolute instability conditions of the surface layer in the Milan Summer, Po Valley Spring (12:00 GMT) and Po Valley Summer (12:00 GMT) models.

4. – Calculations of the upward radiance flux in different atmospheric models

The computer code LOWTRAN 7 [16] is suitable for use with all the atmospheric models described above. Each atmospheric model provides the vertical distribution curves of temperature, air pressure and moisture parameters in the altitude range from 0 to 100 km: these profiles can be divided by the LOWTRAN 7 [16] code into no more than thirty-three layers of variable depths. For each layer, the transmittance sub-routines furnish the spectral curves of partial transmittance due to the various atmospheric constituents as a function of wave number ν (given by the inverse of wavelength measured in cm), with a spectral resolution of 5 cm^{-1} in the wave number range from 350 to 40000 cm^{-1}, which corresponds to the 0.25–28.6 μm wavelength interval. The LOWTRAN 7 code assumes that i) each atmospheric layer is isothermal and presents a temperature value calculated as the average between the temperatures defined at the two extreme levels of the layer, and ii) each atmospheric layer has emittance equal to the absorptance (according to Kirchhoff's law) and, hence, to the difference between unity and the partial transmittance of the layer calculated for the absorption processes only, which are due to both gases and aerosols. Thus, using the LOWTRAN 7 [16] code for all the 23 atmospheric models, it is possible to calculate the spectral curves of the radiance emitted upward by the various atmospheric layers, as well as those of the upwelling radiance reaching the outer space. In order to study the dependence features of temperature deficit ΔT on the various thermodynamic and composition parameters of the atmosphere, one can then calculate the spectral distribution curves of upward radiance $R(\nu)$ in the 2500.00–2857.14 cm^{-1} wave number range, which corresponds to the 3.5–4.0 μm wavelength range, determining the monochromatic values of $R(\nu)$ in wave number steps of 5 cm^{-1}, for all the 23 models in table I.

In carrying out these computations for each atmospheric model, the following two assumptions were made:

i) The surface temperature T_s is equal to the air temperature T_0 at ground level. This assumption is not far from the reality for most cases in maritime areas, but it often appears to be unrealistic in areas where the terrain is subject to strong diurnal heating by solar radiation or is affected by intense radiative cooling during the night.

ii) The surface behaves as a perfect black body and, therefore, its emittance is equal to unity. This assumption is quite realistic in maritime areas, but somewhat unrealistic in continental areas, since the absolute emittance of the terrain is estimated to vary usually between 0.93 and 0.98 in the 3.5–4.0 μm spectral range [9].

The LOWTRAN 7 [16] code divides the atmosphere into a limited number ($\leqslant 33$) of isothermal layers of variable depths from the surface level to 100 km height, and calculates the water vapour content of each layer from the values of absolute humidity determined at the two extreme levels of the layer. Thus, in order to 1) obtain realistic calculations of the upward radiance flux for different vertical profiles of temperature and absolute humidity, and 2) evaluate the importance of the errors due to the choice of the criteria adopted for subdividing the atmosphere into several isothermal layers, we decided to use

three different schemes of vertical subdivision of the atmosphere, as defined by the three series of significant levels in table II:

1) series A, which establishes 32 layers from sea level to 100 km height, according to the subdivision scheme chosen in the original version of the LOWTRAN 7 [16] code, defining 25 layers of 1 km depth from the sea level to the 25 km height, 5 layers of 5 km depth from 25 to 50 km, the penultimate layer from 50 to 70 km and the last layer from 70 to 100 km;

2) series B, which defines an overall number of 29 atmospheric layers from the sea level to 100 km, so as to i) increase the number of layers below the 5 km altitude, where the atmosphere presumably presents stronger absorption conditions for the infrared radiation and, hence, more intense thermal emission, and ii) reduce the number of layers in the upper atmospheric region, where the absorption is in general considerably weaker than that usually occurring in the low troposphere; and

3) series C, which defines 33 layers in all, 21 of which are situated below the altitude of 6 km and only 8 layers are used to represent the thermodynamic features of the stratospheric and mesospheric regions, from 10 to 100 km.

The subdivision scheme described by series C was chosen in order to focus on the emission processes occurring in the lower troposphere, and necessarily neglects the thermal radiation emission occurring in the upper part of the troposphere. Particular attention was also paid to the role played by aerosol particle polydispersions, taking into account that the aerosol radiative effects are more intense in the lower troposphere. Moreover, in order to represent the airborne aerosol extinction effects more realistically, we decided to use the aerosol models determined by Shettle and Fenn [19] for particle polydispersions of rural, urban, maritime and tropospheric origins:

i) the tropospheric aerosol extinction model presents a monomodal size-distribution curve of log-normal shape, where the mode radius gradually increases as a function of the relative humidity of air, the aerosol particles being composed by a mixture of water-soluble and dust-like substances;

ii) the rural aerosol extinction model presents a bimodal size-distribution curve, in which the first mode has a log-normal shape and consists of tropospheric aerosol particles, and the second has a log-normal shape and consists of large rural aerosols containing water-soluble substances (ammonium and calcium sulphate, together with organic compounds) for the 70% of the total mass and dust-like particulate matter for the remaining 30%;

iii) the maritime aerosol extinction model presents a bimodal size distribution curve consisting of a log-normal mode of tropospheric aerosol particles and a log-normal mode of oceanic aerosol particles (sea-salt solution droplets);

iv) the urban aerosol extinction model presents a bimodal size-distribution curve, in which the first mode is given by a log-normal size distribution curve of small aerosol particles having a similar shape to that of the tropospheric model, and the second mode is represented by a log-normal polydispersion of large aerosol particles: in both modes, the aerosol particles were assumed to be a mixture of rural aerosol (for the 80% of the total mass) and carbonaceous (soot-like) aerosol (for the residual 20%).

In all these aerosol extinction models, the visual range V_0 at ground level was assumed to vary from 5 km (hazy conditions) to 23 km (clean air conditions), correspondingly

TABLE II. – *Series A, B and C of significant levels selected in order to subdivide the atmosphere into isothermal layers for calculations of the upwelling radiance within the 3.5–4.0 μm spectral range, using the LOWTRAN 7 [16] computer code.*

Level	Height z (km)		
number	Series A	Series B	Series C
1	0.0	0.0	0.0
2	1.0	0.5	0.1
3	2.0	1.0	0.2
4	3.0	1.5	0.3
5	4.0	2.0	0.4
6	5.0	2.5	0.6
7	6.0	3.0	0.8
8	7.0	3.5	1.0
9	8.0	4.0	1.2
0	9.0	4.5	1.4
11	10.0	5.0	1.6
12	11.0	6.0	1.8
13	12.0	7.0	2.0
14	13.0	8.0	2.2
15	14.0	9.0	2.6
16	15.0	10.0	3.0
17	16.0	12.0	3.5
18	17.0	14.0	4.0
19	18.0	16.0	4.5
20	19.0	18.0	5.0
21	20.0	20.0	5.5
22	21.0	22.0	6.0
23	22.0	25.0	7.0
24	23.0	30.0	8.0
25	24.0	35.0	9.0
26	25.0	40.0	10.0
27	30.0	45.0	12.0
28	35.0	50.0	14.0
29	40.0	70.0	16.0
30	45.0	100.0	20.0
31	50.0	–	30.0
32	70.0	–	40.0
33	100.0	–	50.0
34	–	–	100.0

producing different values of the aerosol optical thickness $\tau_a(\lambda)$ at visible and infrared wavelengths, while the columnar aerosol mass content varies with aerosol optical thickness and particulate matter composition. For instance, on the basis of computations carried out according to the results obtained by Shettle and Fenn [19], Elterman [42], Tomasi [43] and Tomasi and Vitale [44] for rural aerosol particles, we found that optical thickness $\tau_a(0.55\ \mu$m) is equal to 0.235 and 0.780 for values of the visual range V_0 equal to 23 and 5 km, respectively. Correspondingly, the vertical mass loading of aerosol particles was found to be equal to 0.074 gm^{-2} for $V_0 = 23$ km and to 0.247 gm^{-2} for $V_0 = 5$ km. These results clearly indicate that the particulate mass content in the vertical atmospheric
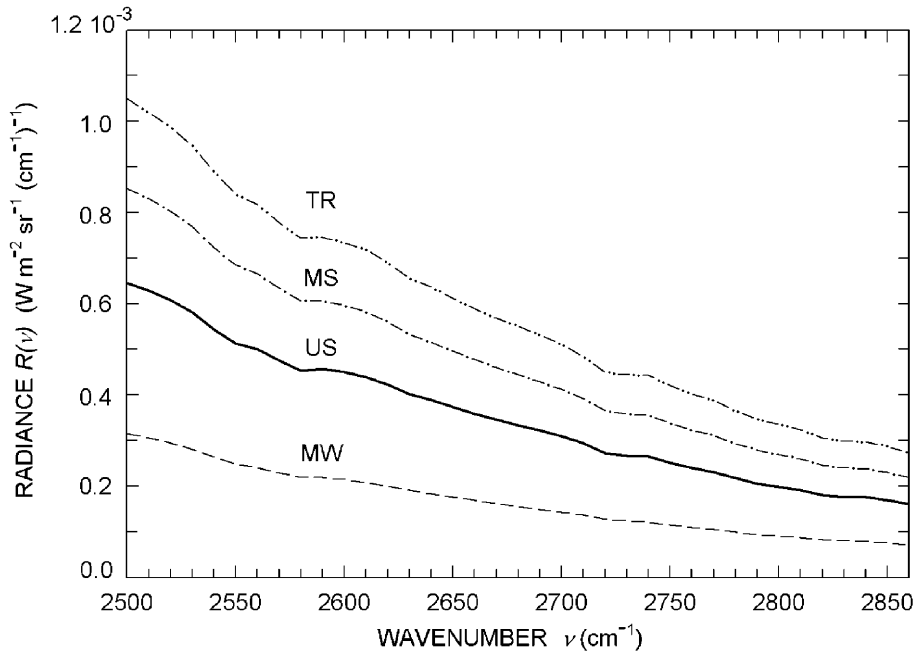
Fig. 3. – Spectral curves of the upwelling radiance $R(\nu)$ calculated in the wave number range from 2500 to 2860 cm^{-1} (*i.e.* within the wavelength range from 4.0 to about 3.5 μm, respectively) for the following four atmospheric models [17]: Tropical (TR), Mid-latitude Summer (MS), US Standard Atmosphere 1976 (US), and Mid-latitude Winter (MW). Each of the four atmospheric models was subdivided into 32 isothermal layers defined by the significant levels listed in series A of table II. In all models, aerosol particle extinction was calculated in terms of the bimodal size-distribution model of rural aerosol particles [19], normalised to visual range $V_0 = 23$ km at ground level.

column of unit cross-section can increase considerably, for instance by a factor equal to about 3.2 in the case of the rural aerosol extinction model, as one passes from high visual range conditions to hazy conditions at ground level.

5. – Computation of the temperature deficit

Using the LOWTRAN 7 [16] code within the 3.5–4.0 μm wavelength range for all the atmospheric and physical models described in the previous sections, we determined the spectral distribution curves of radiance $R(\nu)$ emitted upward in the vertical direction by the surface-atmosphere system. Figure 3 shows the spectral radiance curves obtained for four atmospheric models chosen among those defined by McClatchey *et al.* [17], which were subdivided into the isothermal layers defined by the series A of significant levels and normalised to $V_0 = 23$ km for the rural aerosol extinction model [19]. Precipitable water w changes from one atmospheric model to another, increasing from 0.85 g cm^{-2} (model MW) to 4.12 g cm^{-2} (model TR), while aerosol extinction parameters were assumed to be the same in all four cases. Thus, fig. 3 shows very clearly that the spectral upward radiance $R(\nu)$ increases considerably at all the wave numbers ν as the atmospheric content of water vapour increases from low values typical of mid-latitude
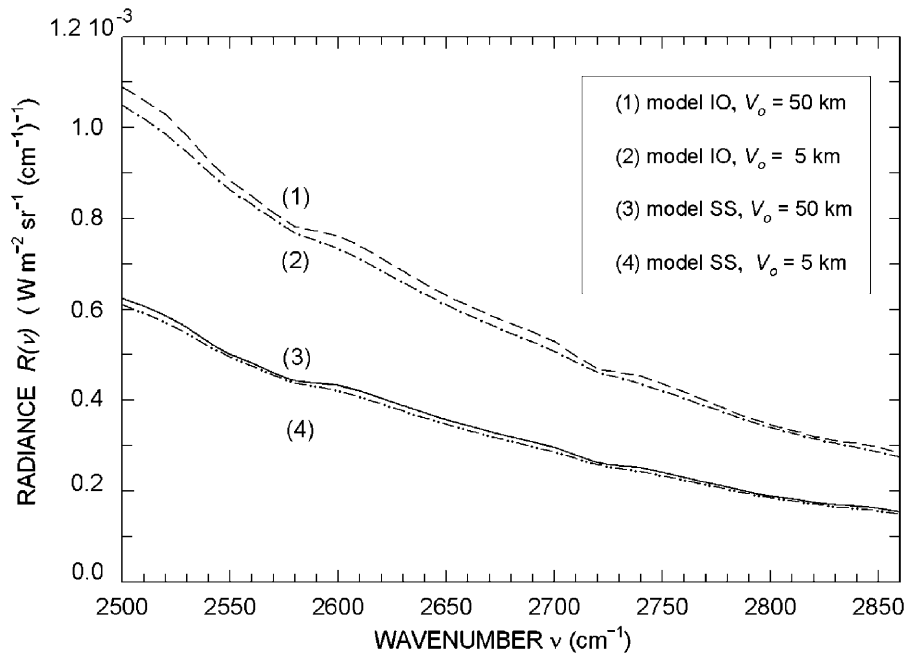
Fig. 4. – Spectral curves of upwelling radiance $R(\nu)$ calculated in the wave number range from 2500 to 2860 cm^{-1} for the following four cases, in which the aerosol extinction was represented in terms of the maritime aerosol particle model [19] normalised to two different values of the visual range V_0 at sea level: 1) Indian Ocean (IO) model [40,41] with $V_0 = 50$ km, 2) model IO with $V_0 = 5$ km, 3) Subarctic Summer (SS) model [17] with $V_0 = 50$ km, and 4) model SS with $V_0 = 5$ km. Each atmospheric model was subdivided into 33 isothermal layers defined by the significant levels listed in series C of table II.

winter conditions to high values typical of atmospheres presenting warm and humid air conditions in their lower part.

Figure 4 presents the spectral curves of $R(\nu)$ obtained for the Indian Ocean (IO) and Subarctic Summer (SS) models with values of V_0 equal to 5 and 50 km: these calculations were made using the subdivision scheme C given in table II and representing aerosol particle extinction with the maritime aerosol model [19]. The two curves of $R(\nu)$ determined for model IO turn out to be very similar, presenting considerably higher values than those found for model SS at all wave numbers: the results confirm that water vapour absorption and corresponding emission processes (strongly depending on the thermal conditions of the atmosphere) exert a marked influence on the intensity of upward radiance $R(\nu)$, as pointed out in fig. 3. These remarks suggest that radiance $R(\nu)$ can vary greatly with season and latitude at all the wave numbers and, to a lesser extent, as a consequence of visual range and aerosol optical thickness variations.

Spectral curves of $R(\nu)$ were then calculated over the 3.5–4.0 μm spectral interval for the 23 atmospheric models listed in table I, using the four aerosol particle extinction models described in the previous section and considering different values of visual range V_0 ranging from 5 to 50 km. The calculations were performed using the three schemes A, B and C to subdivide the whole atmosphere into isothermal layers. All the spectral curves were subsequently integrated from 2500 to 2857.14 cm^{-1} in order to calculate

TABLE III. – *Values of upwelling radiance R measured in* $W\ cm^{-2}sr^{-1}\ (cm^{-1})^{-1}$ *and temperature deficit* ΔT *(measured in* K*), obtained for the* 23 *atmospheric models listed in table I (where the aerosol extinction is represented in terms of the rural aerosol model* [19]*, assumed in all models to have visual range* $V_0 = 23$ km *at ground level), by subdividing the atmospheric region from sea level to the* 100 km *height into several isothermal layers, according to the schemes A, B and C shown in table II and the subdivision scheme D adopted by Tomasi et al.* [45, 46].

Model	Scheme A		Scheme B		Scheme C		Scheme D	
number	R	ΔT	R	ΔT	R	ΔT	R	ΔT
1	2.003×10^{-5}	3.44	2.006×10^{-5}	3.41	2.007×10^{-5}	3.40	2.006×10^{-5}	3.41
2	5.876×10^{-6}	1.58	5.881×10^{-6}	1.56	5.883×10^{-6}	1.55	5.880×10^{-6}	1.56
3	1.591×10^{-5}	2.68	1.593×10^{-5}	2.65	1.594×10^{-5}	2.64	1.593×10^{-5}	2.65
4	2.679×10^{-6}	0.85	2.680×10^{-6}	0.84	2.681×10^{-6}	0.83	2.680×10^{-6}	0.84
5	1.166×10^{-5}	2.56	1.168×10^{-5}	2.53	1.169×10^{-5}	2.51	1.168×10^{-5}	2.53
6	1.228×10^{-5}	2.45	1.230×10^{-5}	2.41	1.230×10^{-5}	2.41	1.229×10^{-5}	2.43
7	7.288×10^{-6}	1.31	7.306×10^{-6}	1.26	7.305×10^{-6}	1.27	7.301×10^{-6}	1.28
8	1.720×10^{-5}	3.08	1.722×10^{-5}	3.06	1.723×10^{-5}	3.04	1.719×10^{-5}	3.10
9	2.284×10^{-5}	3.53	2.283×10^{-5}	3.54	2.282×10^{-5}	3.56	2.278×10^{-6}	3.59
10	1.258×10^{-5}	1.99	1.258×10^{-5}	1.99	1.258×10^{-5}	1.99	1.256×10^{-5}	2.03
11	7.298×10^{-6}	1.38	7.324×10^{-6}	1.31	7.338×10^{-6}	1.28	7.334×10^{-6}	1.29
12	8.111×10^{-6}	1.54	8.127×10^{-6}	1.50	8.129×10^{-6}	1.49	8.122×10^{-6}	1.51
13	1.251×10^{-5}	2.39	1.255×10^{-5}	2.33	1.256×10^{-5}	2.30	1.255×10^{-5}	2.33
14	1.546×10^{-5}	2.78	1.547×10^{-5}	2.77	1.548×10^{-5}	2.76	1.544×10^{-5}	2.81
15	1.742×10^{-5}	2.80	1.749×10^{-5}	2.71	1.753×10^{-5}	2.66	1.752×10^{-6}	2.67
16	2.155×10^{-5}	3.20	2.156×10^{-5}	3.19	2.156×10^{-5}	3.19	2.152×10^{-5}	3.23
17	9.330×10^{-6}	1.46	9.363×10^{-6}	1.39	9.384×10^{-6}	1.34	9.378×10^{-6}	1.36
18	1.168×10^{-5}	1.95	1.169×10^{-5}	1.93	1.169×10^{-5}	1.93	1.168×10^{-5}	1.95
19	8.907×10^{-6}	1.76	8.944×10^{-6}	1.67	8.967×10^{-6}	1.62	8.960×10^{-6}	1.64
20	8.446×10^{-6}	1.57	8.487×10^{-6}	1.48	8.506×10^{-6}	1.43	8.499×10^{-6}	1.45
21	1.181×10^{-5}	2.29	1.183×10^{-5}	2.24	1.184×10^{-5}	2.23	1.183×10^{-5}	2.24
22	1.100×10^{-5}	2.12	1.103×10^{-5}	2.06	1.105×10^{-5}	2.03	1.103×10^{-5}	2.06
23	2.021×10^{-5}	3.81	2.024×10^{-5}	3.78	2.025×10^{-5}	3.76	2.024×10^{-5}	3.78

the overall upward radiance R reaching outer space within this spectral interval. The values of R were subsequently compared with those obtained from the spectral radiance curves determined in terms of the black-body emission theory for a set of plane bodies having temperatures increasing gradually from 243 to 313 K, in steps of 0.1 K. From the comparison, we obtained precise evaluations of the equivalent brightness temperature T_b for all the values of R obtained for the 23 atmospheric models listed in table I. We then calculated the values of temperature deficit ΔT in terms of eq. (1) for all these cases, relative to the three subdivision schemes A, B and C given in table II, where the aerosol extinction was represented in terms of the rural aerosol model [19] normalised to the visual range $V_0 = 23$ km at ground level. Similar calculations were also made using a computer programme in which the LOWTRAN 7 code can be used repeatedly by means of a loop series based on the subdivision scheme D adopted by Tomasi *et al.* [45, 46], defining an overall number of 324 isothermal layers having depths increasing with altitude, in the height range from 0 to 100 km. These last values of upwelling radiance R and temperature deficit ΔT were found to be very close to those calculated

TABLE IV. – *Values of absolute (second column) and relative differences (third column) between the radiance values R_C and R_D, determined for the 23 atmospheric models listed in table I, using the subdivision schemes C and D, respectively. The corresponding absolute and relative differences between the values of temperature deficit ΔT for the two subdivision schemes C and D are given in the fourth and fifth columns, respectively.*

Model number	$R_C - R_D$ (W cm^{-2}sr^{-1} (cm^{-1})$^{-1}$)	$(R_C - R_D)/R_C$	$\Delta T_C - \Delta T_D$ (K)	$(\Delta T_C - \Delta T_D)/\Delta T_C$
1	1×10^{-8}	0.5×10^{-3}	-0.01	-2.9×10^{-3}
2	3×10^{-9}	0.5×10^{-3}	-0.01	-6.4×10^{-3}
3	1×10^{-8}	0.6×10^{-3}	-0.01	-3.8×10^{-3}
4	1×10^{-9}	0.4×10^{-3}	-0.01	-1.2×10^{-2}
5	1×10^{-8}	0.9×10^{-3}	-0.02	-7.9×10^{-3}
6	1×10^{-8}	0.8×10^{-3}	-0.02	-8.2×10^{-3}
7	4×10^{-9}	0.6×10^{-3}	-0.01	-7.8×10^{-3}
8	4×10^{-8}	2.3×10^{-3}	-0.06	-1.9×10^{-2}
9	4×10^{-8}	1.8×10^{-3}	-0.03	-8.4×10^{-3}
10	2×10^{-8}	1.6×10^{-3}	-0.04	-2.0×10^{-2}
11	4×10^{-9}	0.6×10^{-3}	-0.01	-7.8×10^{-3}
12	7×10^{-9}	0.9×10^{-3}	-0.02	-1.3×10^{-2}
13	1×10^{-8}	0.8×10^{-3}	-0.03	-1.3×10^{-2}
14	4×10^{-8}	2.6×10^{-3}	-0.05	-1.8×10^{-2}
15	1×10^{-8}	0.6×10^{-3}	-0.01	-3.7×10^{-3}
16	4×10^{-8}	1.9×10^{-3}	-0.04	-1.2×10^{-2}
17	6×10^{-9}	0.6×10^{-3}	-0.02	-1.5×10^{-2}
18	1×10^{-8}	0.9×10^{-3}	-0.02	-1.0×10^{-2}
19	7×10^{-9}	0.8×10^{-3}	-0.02	-1.2×10^{-2}
20	7×10^{-9}	0.8×10^{-3}	-0.02	-1.4×10^{-2}
21	1×10^{-8}	0.9×10^{-3}	-0.01	-4.5×10^{-3}
22	2×10^{-8}	1.8×10^{-3}	-0.03	-1.5×10^{-2}
23	1×10^{-8}	0.5×10^{-3}	-0.02	-5.3×10^{-3}

using the three subdivision schemes given in table II. All the values of upwelling radiance R and temperature deficit ΔT obtained for the 23 atmospheric models listed in table I are given in table III, as determined for the visual range $V_0 = 23$ km relative to the rural aerosol model [19]. The results show that very small discrepancies exist among the values of R and among those of ΔT obtained using the subdivision schemes A, B, C and D. For instance, considering the absolute and relative differences presented in table IV between the values of R and ΔT obtained using the subdivision schemes C (with 34 isothermal layers) and D (with 324 isothermal layers), it can be noticed that the differences between the radiance evaluations do not exceed the value of 4×10^{-8} W cm^{-2} sr^{-1} (cm^{-1})$^{-1}$, as in the case of the Po Valley Spring (12:00 GMT) model, which corresponds to a relative variation smaller than 0.26%. Similarly, the values of parameter ΔT determined using the more detailed scheme D were found to be higher than those obtained with scheme C by no more than 0.06 K, presenting relative differences between the estimates of ΔT ranging from -0.29% (model TR) to -2.0% (Milan Autumn model).

The agreement between the results obtained using different subdivision schemes is also confirmed by the results shown in fig. 5, where the values of ΔT given in table III are plotted *vs.* the precipitable water values determined in table I for the various atmospheric

models. Best-fit lines in the form of the following equation:

$$(2) \qquad\qquad \Delta T = a_0 + a_1 w,$$

were also drawn in fig. 5, providing very similar values of intercept a_0 and slope coefficient a_1. As can be seen, the regression lines determined for the four sets of values of ΔT are very close one to another. For example, the best-fit line found for the data-set defined using the subdivision scheme C is given by the pair $a_0 = 1.15$ K and $a_1 = 0.61$ K g^{-1}cm^2, with a regression coefficient of $+0.71$, while the best-fit line determined for the data-set given by the scheme D was found for $a_0 = 1.17$ K, $a_1 = 0.61$ K g^{-1}cm^2 and regression coefficient of $+0.70$. Examining the values of a_0 and a_1 obtained in fig. 5 for the four best-fit lines, one finds that the dependence features of ΔT on precipitable water can be realistically examined also by using the three subdivision schemes A, B and C, based on the use of a limited number of isothermal layers. However, this is true only in cases where the atmospheric models are characterised by continuous features of the vertical profiles of temperature and absolute humidity and do not present abrupt and large changes of the thermodynamic parameters with height. Bearing in mind that discontinuity features can take place very frequently in reality, often within layers of limited depth, we decided to use the sub-division scheme D in further calculations aimed at investigating the dependence features of ΔT on the meteorological and composition parameters of the atmosphere.

The results shown in fig. 5 clearly indicate that the temperature deficit ΔT increases very steeply as a function of precipitable water. It assumes values ranging between 1 and 2 K in atmospheric models characterised by cold and relatively dry air conditions of the low troposphere (with precipitable water w ranging between 0.42 and 1.28 g cm^{-2}) and exhibits values higher than 3 K in models characterised by warm and humid air conditions within the lower tropospheric region (giving values of w ranging between 2.07 and 5.11 g cm^{-2}). However, the data-points in fig. 5 are widely scattered, suggesting that a close linear relationship between ΔT and w cannot be found for such an inhomogeneous set of atmospheric models, characterised by greatly varying thermal conditions of the troposphere and features of the vertical distribution curve of absolute humidity. The results shown in fig. 5 turn out to be very similar to those determined by Grassl [47], who examined the dependence characteristics of temperature deficit on the water vapour content of the US Standard Atmosphere [17] in the AVHRR channels 4 and 5, centred at 11 μm and 12 μm wavelengths, respectively. He explained these dependence features not only in terms of water vapour absorption, but also of variations in the vertical distribution curves of air temperature. In particular, he pointed out that: i) the temperature deficit ΔT assumes lower values in cold atmospheres than in warm atmospheres, even though precipitable water w does not change; ii) ΔT increases as a function of w, presenting very low values of the slope-coefficient in atmospheres characterised by nocturnal cooling effects within the ground layer; and iii) ΔT increases with w, presenting gradually higher values of the slope-coefficient as the atmospheric ground layer becomes warmer, as a consequence of ground heating due to solar radiation.

Similar results were also found by Tomasi *et al.* [45] on the basis of preliminary calculations of the ΔT variations due to precipitable water w, within the AVHRR channels 3, 4 and 5, performed assuming that different temperature gradients formed within the ground layer of 0.3 km depth in the US Standard Atmosphere [17].

Taking these results into account, we decided to examine more closely the dependence features of temperature deficit ΔT on 1) the shape of the vertical profile of temperature within the ground layer, and 2) precipitable water. Moreover, considering that ΔT can
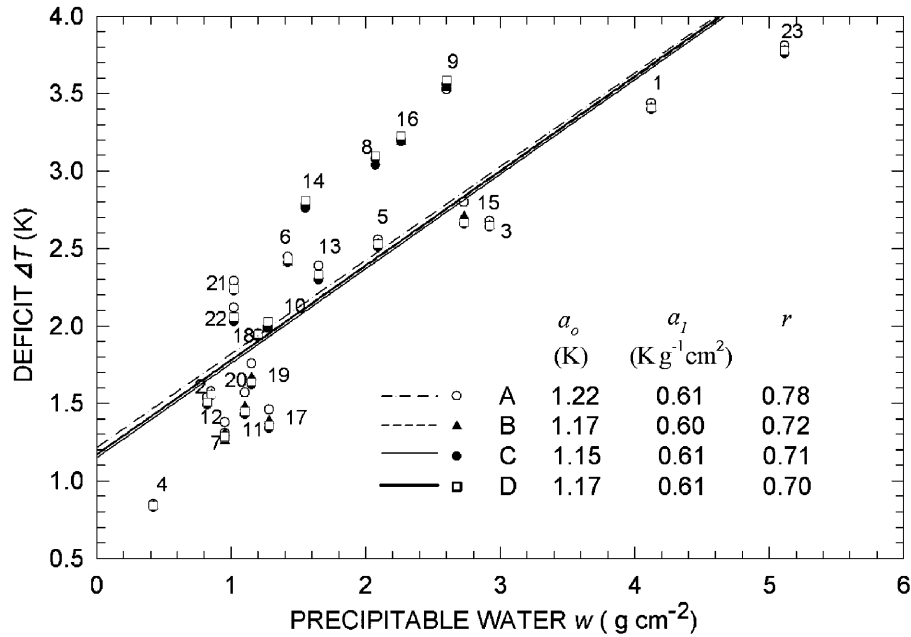
Fig. 5. – Values of temperature deficit ΔT as a function of precipitable water w, as obtained for the 23 atmospheric models listed in table I and labelled with the same numbers used in table I. The atmospheric models were subdivided into horizontal layers according to the vertical subdivision schemes defined in table II by series A (open circles), series B (solid triangles), series C (solid circles) and scheme D adopted by Tomasi et $al.$ [45, 46] (open squares), which divides the atmospheric region from 0 to 100 km height into 324 isothermal layers. The corresponding four best-fit lines defined in the form of eq. (2) were found to differ very little, presenting very close values of intercept a_0, slope coefficient a_1 and regression coefficient r, as can be seen in the figure itself. These results indicate that the evaluations of ΔT obtained using the subdivision scheme C are in practice fully reliable, to an extent comparable with that of scheme D.

be also appreciably modified by other extinction processes occurring in the atmosphere, such as aerosol extinction and absorption by minor gases, we also examined the dependence features of ΔT on i) the variations in the aerosol optical thickness and radiative properties, and ii) the changes in the mean atmospheric concentrations of the minor gases presenting marked absorption features within the 3.5–4.0 μm spectral range, such as methane and nitrous oxide.

6. – Dependence of temperature deficit on the thermal characteristics of the atmosphere

To determine the dependence features of temperature deficit ΔT on the vertical distribution characteristics of air temperature $T(z)$ within the atmospheric ground layer, we calculated the values of ΔT following the procedure described in the previous section and based on the use of the subdivision scheme D [45,46]. Six sets of atmospheric models were considered, each set being obtained from one of the six atmospheric models called TR, MW, MS, SW, SS and US in table I [17]. The six sets were determined by modifying the six vertical profiles of air temperature proposed by McClatchey et $al.$ [17], as follows:

i) for each original model, we fixed six values of height z_j increasing from 0.1 to 0.6 km, in steps of 0.1 km;

ii) for each value of z_j, we assumed that the vertical profile of temperature at the altitudes higher than z_j is the same given by the original model of McClatchey *et al.* [17];

iii) at altitudes $z \leqslant z_j$, we assumed that temperature $T(z)$ takes the value given by the original model at height z_j and increasing or decreasing values with height at all the underlying levels from z_j to the sea-level: these values of air temperature were calculated for 13 different values of the temperature gradient $\gamma = \mathrm{d}T(z)/\mathrm{d}z$, assumed to vary from -20 to 40 K/km, in steps of 5 K/km.

We obtained a set of 78 vertical profiles of air temperature within the ground layer for each of the six above-chosen atmospheric models, correspondingly finding 78 different values of the surface temperature T_s. Moreover, we assumed that all the 78 atmospheric configurations relative to each atmospheric model were characterised by the same value of precipitable water w, assumed to be equal to that given by the original model (see table I). This was done by appropriately modifying the relative humidity conditions at all the levels within the ground layer $z \leqslant z_j$, in such a way as to impose constant percentage variations of relative humidity f at all the significant levels of the ground layer, then uniformly lowering or increasing the original values of f in all the 78 cases.

For the overall 468 atmospheric configurations defined for the six atmospheric models, we then calculated the corresponding values of temperature deficit ΔT, by assuming specifically that the ground temperature is equal to the surface-level air temperature T_s defined through the above assumptions of parameters z_j and γ. Figure 6 presents the values of ΔT obtained for model US, in which the above-fixed six values of height z_j and the 13 values of temperature gradient γ have been imposed. The results show that ΔT gradually decreases as gradient γ increases, presenting negative slopes, whose absolute values increase appreciably as z_j raises from 0.1 to 0.6 km and become gradually more pronounced passing from negative to positive values of γ. Only in the cases with $z_j = 0.1$ km and $z_j = 0.2$ km, were the results found to follow closely linear dependence patterns, clearly indicating that ΔT can be realistically assumed to vary linearly as a function of temperature gradient γ in cases where the inversion layer at the ground has a limited depth.

Figure 7 presents the 468 values of ΔT obtained for the six models of McClatchey *et al.* [17] as a function of the surface temperature T_s, separately for each model. The values of ΔT calculated for each model were found to increase as a function of T_s, following very closely the patterns described by a polynomial curve throughout the corresponding range of T_s. Relatively low and mostly negative values of ΔT were obtained for cold atmospheric conditions of the ground layer, such as those represented by the configurations defined for models SW and MW, which both present strong temperature inversions near the ground. Higher and positive values of ΔT were found for warmer conditions of the ground layer, as in the configurations obtained from models MS and TR for negative values of γ that yield values of T_s higher than 285 K, *i.e.* in the presence of adiabatic or super-adiabatic conditions of the thermal gradient within the ground layer. Six best-fit polynomial curves of the second order were determined for the six sets of atmospheric configurations shown in fig. 7 in terms of the following equation:

$$\text{(3)} \qquad \Delta T = b_0 + b_1 T_s + b_2 T_s^2 \,,$$

with ΔT and T_s measured in K. The best-fit values of coefficients b_0, b_1 and b_2 are
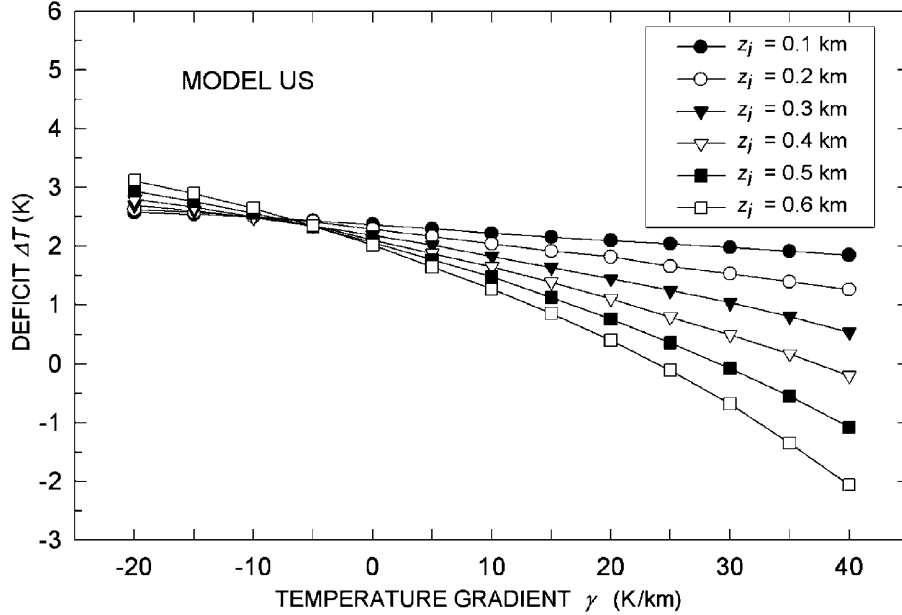
Fig. 6. – Dependence curves of temperature deficit ΔT on temperature gradient γ assumed in the ground layer of atmospheric model US, as found in the 3.5–4.0 μm spectral range for 78 different vertical profiles of temperature. The profiles were obtained by modifying the original vertical profile of temperature given by model US through the assumption of six different values of parameter z_j, equal to 0.1, 0.2, 0.3, 0.4, 0.5 and 0.6 km, and 13 values of temperature gradient γ, ranging from -20 K/km to 40 K/km in steps of 5 K/km. The relative humidity conditions of the ground layer were also appropriately modified within the first 2 kilometres of the atmosphere, to obtain a constant value of precipitable water $w = 1.42$ g cm^{-2} for all the 78 vertical profiles of air temperature.

TABLE V. – *Best-fit values of coefficients b_0, b_1 and b_2 defining the polynomial curves with the analytical form of eq. (3), as found for the six sets of values of temperature deficit ΔT obtained for the six atmospheric models shown in fig. 7.*

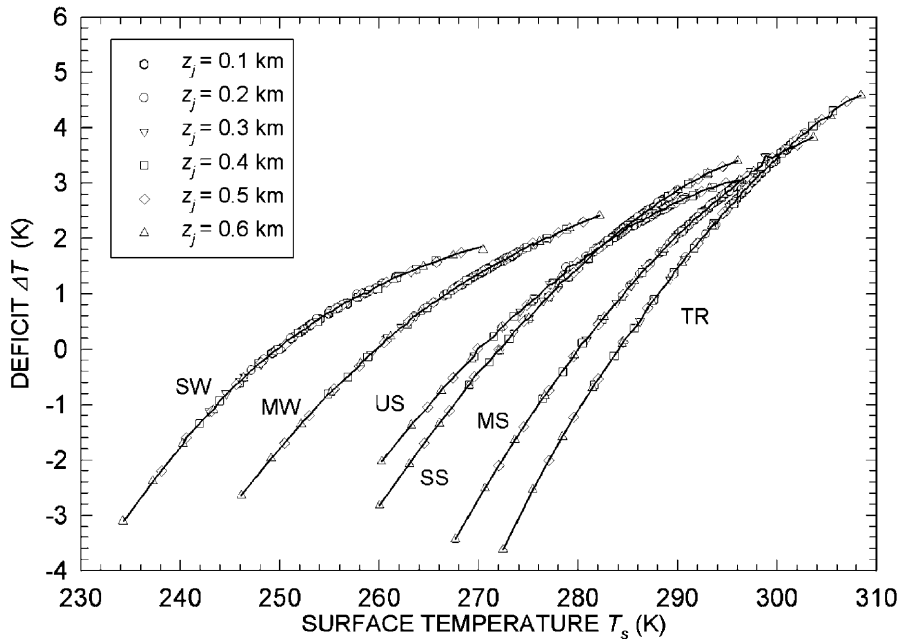| Atmospheric models	b_0 (K)	b_1	b_2 (K^{-1})	Regression coefficient r
Tropical (TR)	-329.1	2.05	-3.1×10^{-3}	0.99995
Mid-latitude Winter (MW)	-203.9	1.41	-2.4×10^{-3}	0.9999
Mid-latitude Summer (MS)	-308.6	1.97	-3.1×10^{-3}	0.99995
Subarctic Winter (SW)	-223.7	1.64	-3.0×10^{-3}	0.9998
Subarctic Summer (SS)	-248.7	1.62	-2.6×10^{-3}	0.9999
US Standard Atmosphere 1976 (US)	-230.2	1.52	-3.0×10^{-4}	0.9999

Fig. 7. – Values of temperature deficit ΔT plotted as a function of surface temperature T_s, as found for six sets of atmospheric models obtained by modifying the vertical profiles of temperature and the moisture characteristics of atmospheric models TR (Tropical), MW (Mid-latitude Winter), MS (Mid-latitude Summer), SW (Subarctic Winter), SS (Subarctic Summer), and US (US Standard Atmosphere 1976), as follows: each set was determined by changing the original vertical profile of air temperature through the assumption of the six values of height z_j listed in the figure and the 13 values of temperature gradient γ in the ground layer, already chosen in fig. 6. Moreover, the relative humidity conditions of the ground layer were modified in each atmospheric model in such a way as to obtain the same original value of precipitable water w for all the 78 various configurations. The values of intercept b_0, coefficients b_1 and b_2 found for the polynomial best-fit solutions drawn in the form of eq. (3) and the corresponding values of regression coefficient r are given in table V.

given in table V, together with the corresponding values of the regression coefficient r, all found to be better than 0.999. The values of b_0 were all found to be negative, varying from -329.1 K (model TR) to -203.9 K (model MW) and, hence, increasing as the mean temperature conditions of the atmosphere gradually decrease. Correspondingly, coefficient b_1 was found to assume positive values, varying between 1.41 (model MW) and 2.05 (model TR), and hence increasing in general with the thermal conditions of the atmosphere, while coefficient b_2 assumed negative values ranging between -3.0×10^{-4} K^{-1} (model US) and -3.1×10^{-3} K^{-1} (models MS and TR). The values of ΔT calculated above do not appear to be appreciably scattered in the diagram of fig. 7, since they follow very closely the best-fit curves drawn in the diagram, each curve being obtained for one of the six models of McClatchey *et al.* [17]. Realistic estimates of the mean variations of ΔT can be obtained as a function of T_s, for various latitudes and seasons, by using in eq. (3) the best-fit values of b_0, b_1 and b_2 given in table V for the various models. The results shown in fig. 7 also indicate that considerable variations in the temperature deficit ΔT can be caused by i) formation of more or less marked

temperature inversion profiles within the ground layer, often due to nocturnal cooling, and ii) superadiabatic lapse rate features, due to very intense heating of the ground layer by solar radiation. It is also of interest to note in fig. 7 that the fastest rates of these dependence features have been found in warm atmospheres (models TR and MS) and the slowest ones in cold atmospheres (models SW and MW).

7. – Dependence of temperature deficit on precipitable water

The results shown in fig. 7 were found on the assumption that precipitable water does not change in the 78 configurations of the atmosphere derived from each atmospheric model. Thus, the curves of ΔT plotted in fig. 7 as a function of surface temperature T_s provide the measure of the variations in ΔT due only to changes in the thermal conditions of the atmospheric ground layer, and not to changes in atmospheric water vapour absorption, since precipitable water was assumed not to vary.

This section examines the aspects concerning the dependence features of ΔT on precipitable water. We considered the four models TR, US, MW and SW [17] characterised by warm, cold and temperate conditions of the low troposphere. In each model, we assumed only one value of parameter z_j, equal to 0.4 km, and seven values of the temperature gradient γ, increasing from -20 to $+40$ K/km in steps of $+10$ K/km. Instead of maintaining constant the precipitable water, we assumed various values of relative humidity f within the ground layer of 2 km depth, taking six increasing values of parameter f from 30% to 80% in regular steps of 10%, thus obtaining six increasing and regularly spaced values of w for each value of γ.

For the four sets, each consisting of 42 atmospheric configurations, we then calculated the temperature deficit ΔT following the procedure described in sect. **5** and using the subdivision scheme D [45,46]. The results are shown in fig. 8, where the values of ΔT are plotted as a function of precipitable water w, separately for each atmospheric model and each value of gradient γ. Considering that the absolute values of the regression coefficients of the best-fit lines drawn in fig. 8 are all close to the unity, the findings indicate that parameter ΔT varies almost linearly as a function of w for each atmospheric model and each gradient γ. This is true throughout all precipitable water intervals resulting from the assumptions made above on the humidity conditions of the lower troposphere. Increasing trends of ΔT were found in all four models in correspondence to the negative values of γ, while values of the slope coefficient close to zero or negative were obtained for values of γ higher than 10 K/km, the negative slope becoming gradually steeper as γ increases.

The dependence curves shown in fig. 8 clearly indicate a close relationship between ΔT and w, in accordance with the remarks made in Grassl [47]. The proportionality coefficient between ΔT and w decreases gradually with γ in all the four sets of atmospheric configurations presented in fig. 8, while the intercept also decreases almost regularly, as γ increases on passing from unstable (superadiabatic) to stable conditions of the ground layer. On the basis of these results and bearing in mind that ΔT is proportional to w, we decided to investigate the dependence features of the proportionality coefficient between ΔT and w on the temperature gradient γ. Thus, we calculated the ratio $\Delta T/w$ for all the 468 atmospheric cases considered in fig. 7, relative to the six models TR, MW, MS, SW, SS and US [17] and defined for 6 values of z_j from 0.1 to 0.6 km and 13 values of γ from -20 to $+40$ K/km. The results are shown in fig. 9, separately for each atmospheric model. The relationship curves defined for warm atmospheres (models TR and MS) indicate that ratio $\Delta T/w$ does not change widely as a function of γ, since it presents values
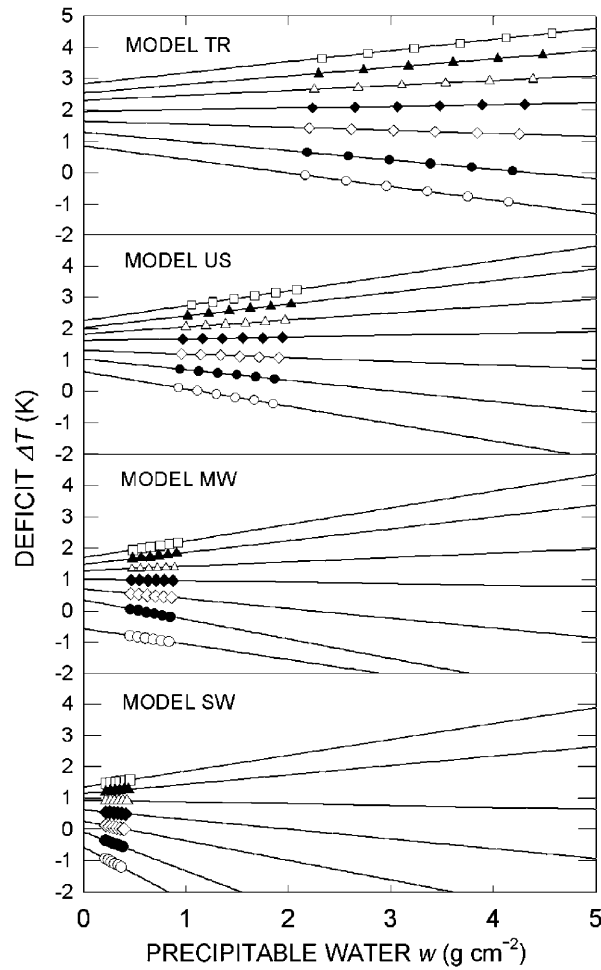
Fig. 8. – Temperature deficit ΔT plotted as a function of precipitable water w, as obtained in the 3.5–4.0 μm spectral range for the atmopheric models TR (Tropical), MW (Mid-latitude Winter), US (US Standard Atmosphere 1976), and SW (Subarctic Winter). Forty-two configurations were obtained for each atmospheric model, by modifying the original vertical profile of air temperature at all the significant levels below height $z_j = 0.4$ km, by assuming i) seven values of temperature gradient γ ranging from -20 K/km (open squares) to $+40$ K/km (open circles) in steps of 10 K/km, and ii) six values of relative humidity within the atmospheric layer from 0 to 2 km height, increasing from 30% to 80% in steps of 10%. Thus, six values of precipitable water w were obtained for each value of γ, obtaining an overall number of 42 different values of w for each model. The corresponding best-fit lines are also drawn for each of the seven values of γ assumed in each atmospheric model.

ranging only between nearly $+1$ and -1 K g^{-1}cm^2. The curves found in the cases with z_j no higher than 0.3 km can be approximated very closely by lines, while those determined for $z_j \geqslant 0.4$ km exhibit gradually more pronounced convex shapes. This increasingly marked trend indicates a growing influence of the thermal features of the atmosphere on ΔT, which gradually increases as level z_j rises becoming at least of 0.3 km.
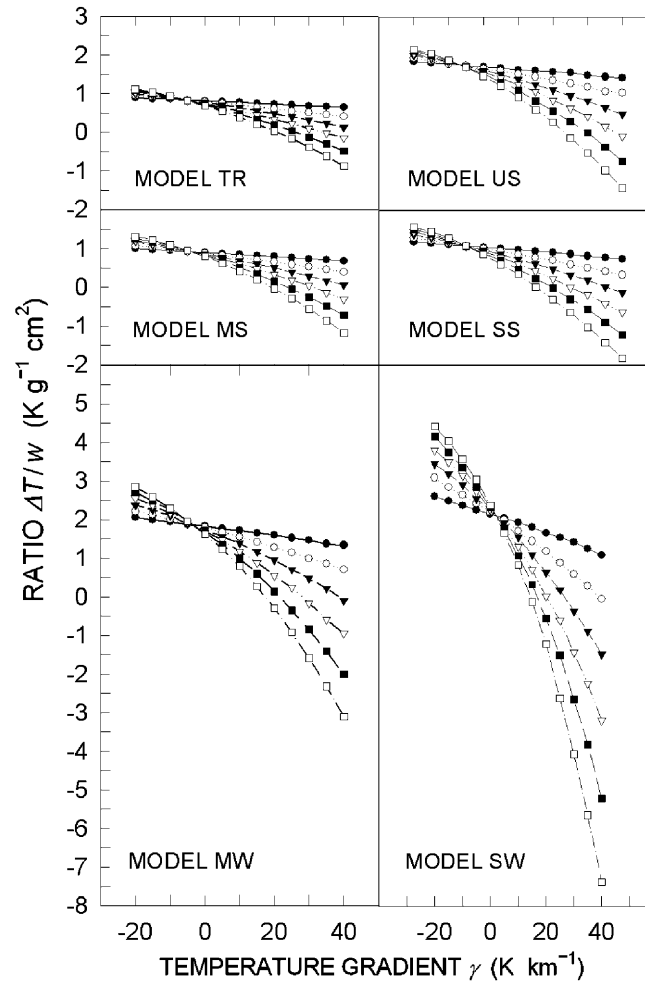
Fig. 9. – Dependence curves of ratio $\Delta T/w$ on temperature gradient γ, as obtained in the 3.5–4.0 μm spectral range for the sets of 78 configurations derived from each of the six atmospheric models SW, SS, MW, US, MS and TR. The vertical profile of air temperature was modified by assuming the above-chosen 6 values of height z_j ranging from 0.1 (solid circles) to 0.6 km (open squares) in steps of 0.1 km and 13 values of temperature gradient γ, increasing from -20 to $+40$ K/km in steps of $+5$ K/km.

The relationship curves found for temperate atmospheres, such as those represented by models US and SS, present values of ratio $\Delta T/w$ varying more widely than those determined in the two previous cases, *i.e.* from $+1.5$ to -2 K g^{-1}cm^2. The curves exhibit more convex shapes than those of models TR and MS, presenting values that gradually increase as z_j becomes higher and γ increases to give form to pronounced temperature inversion profiles. Only in the cases with $z_j = 0.1$ km, can the variations of $\Delta T/w$ as a function of γ be satisfactorily best-fitted by lines. These results indicate that ratio $\Delta T/w$ decreases as i) level z_j increases, *i.e.* as the ground-layer depth becomes larger, and ii) gradient γ increases, *i.e.* as the ground layer becomes more stable. In other words, $\Delta T/w$ lowers as the inversion layer extends and the thermal inversion gets stronger.
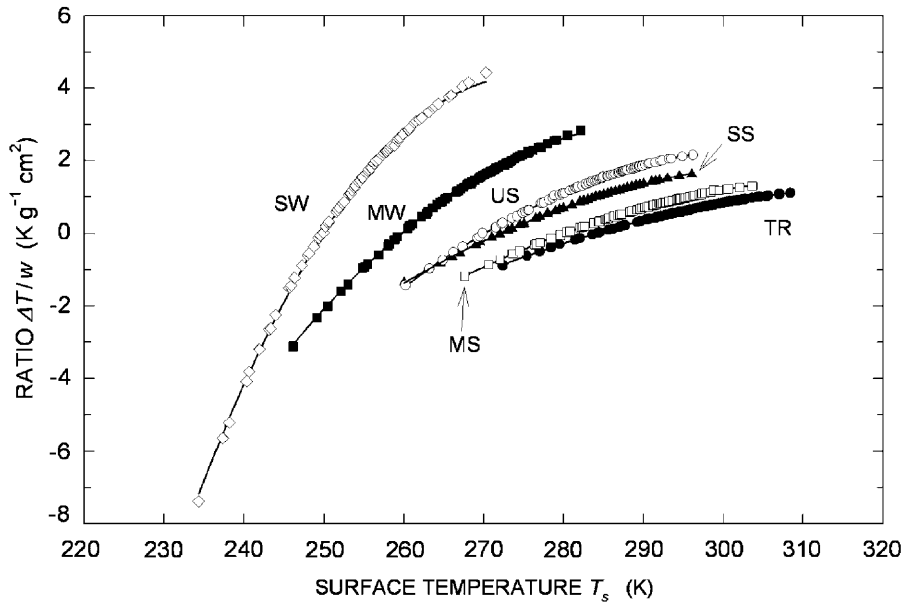
Fig. 10. – Dependence curves of ratio $\Delta T/w$ as a function of surface temperature T_s, obtained for the six atmospheric models shown in fig. 9. Each original atmospheric model was modified by assuming 6 values of height z_j from 0.1 to 0.6 km and 13 values of temperature gradient γ, as in fig. 9. The best-fit values of parameters c_0, c_1 and c_2, defining the polynomial curves drawn for each of the six atmospheric models, are given in table VI, together with the values of regression coefficient r.

In the two cold atmosphere cases considered in fig. 9 (models MW and SW), the dependence features of $\Delta T/w$ on γ turn out to cover even more extensive ranges than in the other four models, since its values were found to vary between $+4.5$ and -7 K g^{-1}cm^2, while the relationship curves present particularly high and variable values of the slope coefficients for positive values of γ and values of z_j greater than 0.3 km. Only in the cases with $z_j = 0.1$ km, was $\Delta T/w$ found to decrease almost linearly with γ, presenting features similar to those of the curves defined for the other four atmospheric models and for the lower values of z_j.

These findings fully confirm the results obtained in fig. 7, indicating that ratio $\Delta T/w$ tends to assume gradually lower values until becoming negative, and considerably lower than -1 K g^{-1}cm^2 in cold atmospheres, as parameter γ assumes positive and higher values and z_j takes the highest values. In other words, the ratio $\Delta T/w$ is expected to become gradually lower and negative, as the surface temperature T_s decreases. Thus, it is important to take into account that ΔT increases with T_s, as has been clearly shown in fig. 7, and that a close dependence relationship exists between ΔT and w, which is a function of parameters z_j and γ, as shown in fig. 8. In order to define analytical forms suitable for representing such dependence features, we reconsidered the calculations of ΔT shown in fig. 7 that were obtained for six atmospheric models [17], 6 values of z_j, 13 values of γ, and only one value of w for each set of 78 atmospheric configurations. The values of $\Delta T/w$ obtained for all the 468 configurations are plotted in fig. 10 as a function of surface temperature T_s, separately for each of the six atmospheric models [17].

TABLE VI. – *Best-fit values of coefficients c_0, c_1 and c_2 defining the polynomial curves with the analytical form of eq. (4), as found for the six sets of values of ratio $\Delta T/w$ obtained for the six atmospheric models shown in fig. 10.*

Atmospheric models	c_0 (K g^{-1}cm^2)	c_1 (g^{-1}cm^2)	c_2 (K^{-1}g^{-1}cm^2)	Regression coefficient r
Tropical (TR)	-79.9	0.498	-8.0×10^{-3}	0.9999
Mid-latitude Winter (MW)	-239.9	1.661	-2.8×10^{-3}	0.9999
Mid-latitude Summer (MS)	-105.7	0.674	-1.1×10^{-3}	0.9999
Subarctic Winter (SW)	-532.5	3.912	-7.1×10^{-3}	0.9996
Subarctic Summer (SS)	-118.9	0.776	-1.2×10^{-3}	0.9999
U.S. Standard Atmosphere 1976 (US)	-162.2	1.072	-1.7×10^{-3}	0.9999

These results agree very well with those found in fig. 9, showing that $\Delta T/w$ varies as a function of T_s, presenting very continuous features. The values of $\Delta T/w$ were found to vary: i) more rapidly in the colder atmospheres (models SW and MW), where a wide range from nearly -8 to about $+4$ K g^{-1}cm^2 turns out to be covered, ii) at slower rates in the temperate atmospheres (models US and SS), where the range of $\Delta T/w$ extends from about -2 to $+2$ K g^{-1}cm^2, and iii) even more slowly in warm atmospheres (models MS and TR), covering a narrower range of $\Delta T/w$ from only -1 to about $+1.5$ K g^{-1}cm^2. Thus, the six relationship curves can be represented with a good approximation by almost linear analytical functions, which were determined as best-fit curves of the six sequences of points drawn in fig. 10 obtained in terms of the polynomial form of the second order,

$$(4) \qquad \Delta T/w = c_0 + c_1 T_\mathrm{s} + c_2 T_\mathrm{s}^2 \,,$$

with ΔT and T_s measured in K and w in g cm^{-2}. The best-fit values of intercept c_0 and coefficients c_1 and c_2 are given in table VI, together with the corresponding values of the regression coefficient r, all found to be better than 0.999. All the values of intercept c_0 are negative, ranging between -532.5 K g^{-1}cm^2 (model SW) and -79.9 K g^{-1}cm^2 (model TR) and, hence, increasing with the air temperature at the top-level of the ground layer. The corresponding values of coefficient c_1 were found to assume positive values varying from 0.498 g^{-1}cm^2 (model TR) to 3.912 g^{-1}cm^2 (model SW) and, therefore, increasing as the atmosphere becomes gradually colder at the ground. Coefficient c_2 was found to assume negative values ranging from -8.0×10^{-4} K^{-1}g^{-1}cm^2 (model TR) to -7.1×10^{-3} K^{-1}g^{-1}cm^2 (model SW), presenting the general tendency to increase as the atmosphere evolves from warm and humid to cold and dry air conditions. Taking into account that the values of $\Delta T/w$ found through the present calculations very closely follow the best-fit curves determined in fig. 10, we can state that realistic evaluations of ratio $\Delta T/w$ can be achieved for various latitudinal and seasonal features of the atmosphere using the relationship curve defined in eq. (4) for the best-fit values of coefficients c_0, c_1 and c_2 given in table VI.
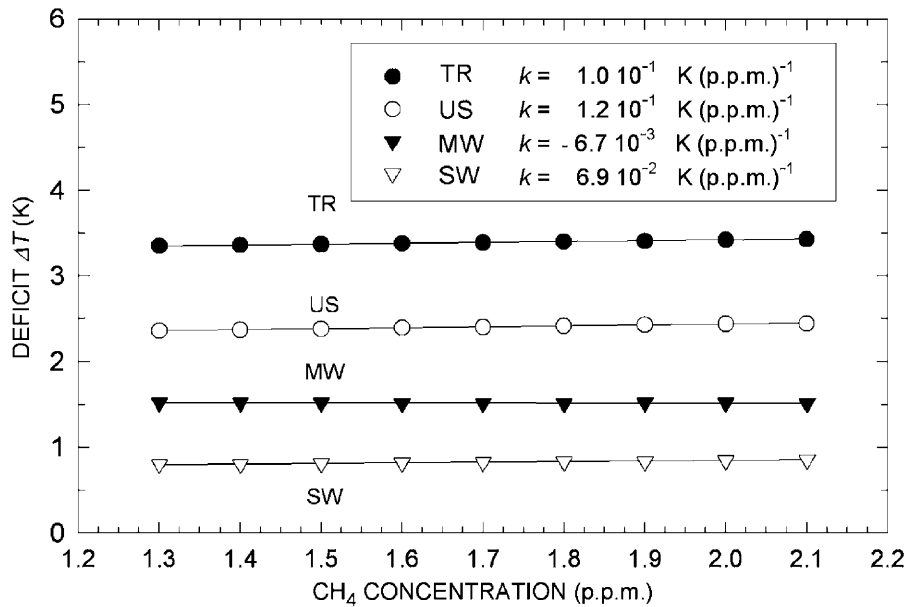
Fig. 11. – Temperature deficit ΔT as a function of the mean atmospheric concentration $C(CH_4)$ of methane, assumed to take nine values increasing from 1.3 to 2.1 p.p.m., in steps of 0.1 p.p.m., within the four atmospheric models TR (Tropical), US (US Standard Atmosphere 1976), MW (Mid-latitude Winter) and SW (Subarctic Winter). The aerosol particle extinction is represented in terms of the rural aerosol extinction model [19], normalised to the visual range $V_0 = 23$ km. The values of the slope coefficient k of the best-fit lines give the measure of the variations of ΔT per unit change in the mean global methane concentration $C(CH_4)$.

8. – Dependence of temperature deficit on methane and nitrous oxide concentrations

As pointed out in sect. **2**, molecules of methane (CH_4) and nitrous oxide (N_2O) absorb very strongly the infrared radiation emitted upward by the terrestrial surface and the various atmospheric layers, within well-defined wavelength intervals of the 3.5–4.0 μm window. This absorption causes appreciable attenuation effects on the overall upwelling radiance measured by the satellite radiometers, which contribute to increase the temperature deficit ΔT within such a spectral range. In order to evaluate the intensity of the effects due to CH_4, we considered the four atmospheric models TR, US, MW and SW [17] representing different latitudinal and seasonal conditions of the atmosphere. We then simulated the aerosol particle extinction in all the four models by means of the rural aerosol extinction model [19] normalised to the visual range $V_0 = 23$ km at ground level. In the four atmospheric models, we assumed that the mean atmospheric methane concentration $C(CH_4)$ increases gradually from 1.3 to 2.1 p.p.m., in regular steps of 0.1 p.p.m.. For all these cases, we calculated the temperature deficit ΔT following the procedure described in sect. **5**. The results are shown in fig. 11, where the values of ΔT are plotted as a function of $C(CH_4)$, separately for each of the four atmospheric models. They indicate that ΔT varies almost linearly with $C(CH_4)$ in all the cases, presenting very low values of the slope coefficient k, varying between -6.7×10^{-3} K $(\text{p.p.m.})^{-1}$ (model MW) and $+1.2 \times 10^{-1}$ K $(\text{p.p.m.})^{-1}$ (model US).
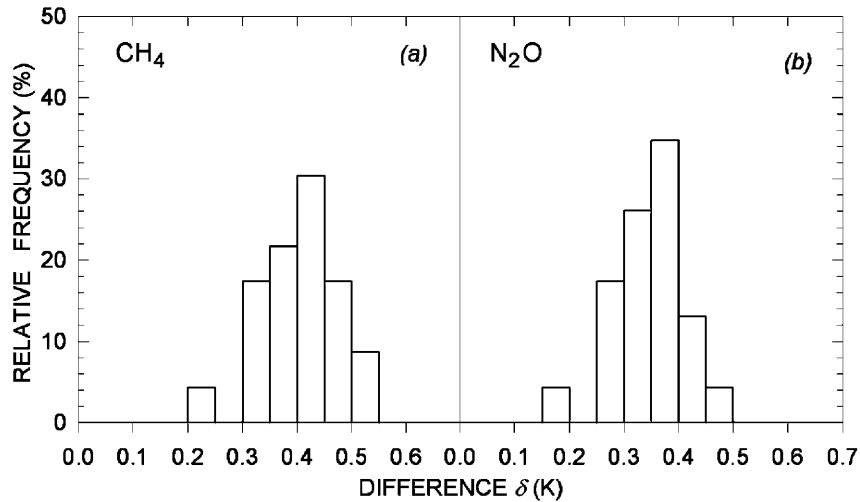
Fig. 12. – a) Relative frequency histogram of the difference δ between the pairs of values of ΔT calculated for the 23 atmospheric models listed in table I, by separately assuming that the mean atmospheric methane concentration $C(\mathrm{CH_4})$ is equal to 1.7 p.p.m. in the first case and 0 p.p.m. in the second one. b) Relative frequency histogram of the difference δ between the pairs of values of ΔT calculated for the 23 atmospheric models in table I, by separately assuming that the mean atmospheric concentration of nitrous oxide $C(\mathrm{N_2O})$ is equal to 0.32 p.p.m. and 0 p.p.m.

Through the procedure defined in sect. **5**, we also calculated the values of temperature deficit ΔT for all the 23 atmospheric models listed in table I, in which $C(\mathrm{CH_4})$ was assumed to be equal to 1.72 p.p.m, *i.e.* to have the mean global concentration value measured over the last years. Thereupon, we calculated the values of ΔT for the same 23 atmospheric models, where $C(\mathrm{CH_4})$ was assumed to be null. Comparing the two series of values of ΔT obtained for all the models with $C(\mathrm{CH_4}) = 1.72$ p.p.m. and $C(\mathrm{CH_4}) = 0$ p.p.m., respectively, we determined the corresponding values of the difference δ between the temperature deficit evaluations made in atmospheres with and without methane. The left part of fig. 12 shows the relative frequency histogram of parameter δ, providing the measure of the partial contribution produced by the present atmospheric concentration of methane on ΔT. As can be seen, the overall range of δ extends from 0.20 to 0.55 K, yielding a median value of δ equal to 0.41 K and the two other quartiles equal to 0.36 and 0.45 K. Examining the overall set of values of δ shown in fig. 12, we found an average value of δ equal to (0.40 ± 0.07) K. Thus, we can state that $\mathrm{CH_4}$ produces a mean temperature deficit per unit variation of its concentration equal to 0.24 K $(\text{p.p.m.})^{-1}$. On the basis of the above quartiles, we estimated that this quantity should vary as a function of the thermal, seasonal and latitudinal characteristics of the atmosphere within an overall range from 0.11 K $(\text{p.p.m.})^{-1}$ (in cold atmospheres) to 0.37 K $(\text{p.p.m.})^{-1}$ (in warm atmospheres), corresponding to $\pm$ three standard deviations.

A similar procedure was also applied to the 23 atmospheric models of table I to obtain a mean estimate of the temperature deficit contribution due to nitrous oxide absorption within the 3.5–4.0 μm window. We calculated ΔT for the models in table I, where the mean global concentration $C(\mathrm{N_2O})$ was assumed to be equal to 0.32 p.p.m. in the first case and to be null in the second case. Then, we calculated the values of the difference

δ between the evaluations of ΔT obtained in atmospheres with and without N_2O. The relative frequency histogram of parameter δ is shown in the right part of fig. 12, covering the range from 0.15 to 0.50 K and presenting a median value of 0.35 K and the two other quartiles equal to 0.31 and 0.39 K. From the overall set of values of δ, we obtained an average value of this parameter equal to (0.35 ± 0.07) K. Considering that the average estimate of the temperature deficit per unit variation of N_2O concentration is equal to 1.1 K $(p.p.m.)^{-1}$ and the mean global concentration of this minor atmospheric constituent is more than five times smaller than that of CH_4, the above findings indicate that N_2O is expected to produce, in reality, a partial ΔT contribution that is slightly weaker than the one produced by atmospheric methane. Moreover, taking into account that ΔT can vary considerably as a function of the thermal, seasonal and latitudinal characteristics of the atmosphere, we can state that ratio $\delta/C(N_2O)$ should cover a relatively wide range from 0.4 to 1.8 K $(p.p.m.)^{-1}$, as one passes from very cold to very warm conditions of the atmosphere, this range being defined taking the mean value plus and minus three times the standard deviation.

In view of these results, the variations in ΔT due to CH_4 and N_2O are expected to be considerably smaller than those caused by atmospheric water vapour and by the thermal characteristics of the atmosphere. Since both CH_4 and N_2O concentrations are subject to vary as a function of latitude and season and from one year to another by a few percentage units [48, 49], the present results indicate that the corresponding changes in ΔT due to these variations can be correctly estimated to be very small, and no higher than a few tenths of Celsius degree, even in extreme cases. However, they can be realistically evaluated and accounted for in the analysis of satellite data, taking into account the estimates of δ presented in fig. 12 for CH_4 and N_2O.

9. – Dependence of temperature deficit on atmospheric aerosols

Mie theory predicts that airborne aerosols of natural and anthropic origins cause the most intense radiative effects on visible radiation, while they extinguish the infrared radiation more weakly, with intensity features that gradually decrease as wavelength increases, in all cases presenting good atmospheric transparency conditions and intensity features nearly stable with wavelength in cases of dense haze or fog layers near the ground. In fact, aerosol particles can cause important attenuation effects on the infrared radiation emitted upward by the terrestrial surface and the overlying atmosphere, when they exhibit relatively high values of optical thickness, mainly due to the presence of significant mass contents of large and giant particles in the vertical atmospheric column. In these particular cases, aerosols can provide an appreciable contribution to the temperature deficit ΔT within the 3.5–4.0 μm wavelength range. In order to evaluate the intensity of such effects, we considered the four atmospheric models MW, MS, US and IO, where the atmospheric aerosol content was assumed to take five intermediate values throughout a rather large range, passing from high visibility to hazy conditions at the ground level with visual range V_0 equal to 50, 23, 15, 10 and 5 km [19, 42, 50], respectively. Correspondingly, the aerosol optical thickness $\tau_a(0.55 \ \mu m)$ was evaluated to present five increasing values equal to 0.152, 0.235, 0.316, 0.432 and 0.780, independent of the origin of particulate matter.

In order to evaluate the aerosol effects for different radiative properties of particulate matter, we represented the aerosol extinction features as follows: i) in model MW, using the monomodal tropospheric aerosol model; ii) in model MS, the bimodal rural aerosol model; iii) in model US, the bimodal urban aerosol model; and iv) in model IO, the
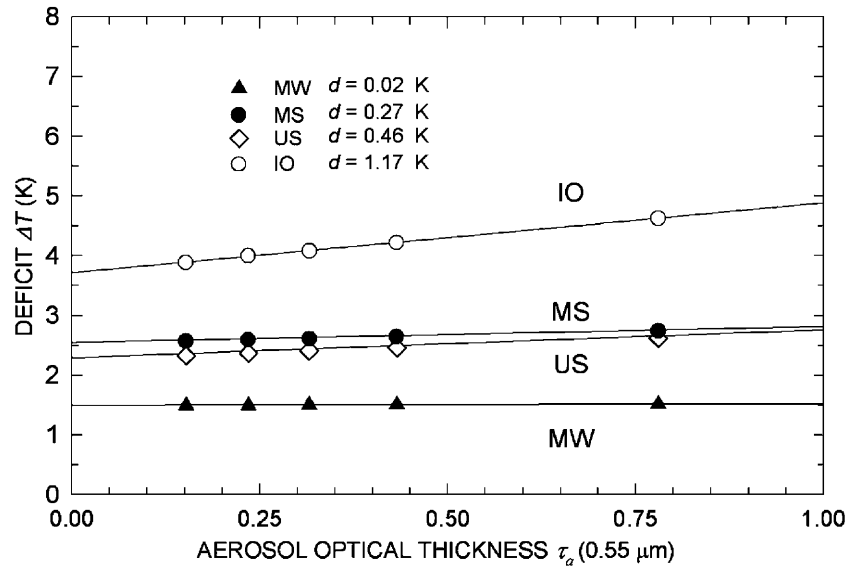
Fig. 13. – Temperature deficit ΔT as a function of aerosol optical thickness $\tau_a(0.55\ \mu\mathrm{m})$ calculated for the four atmospheric models MW, MS, US and IO, using in each model a different aerosol particle extinction model [19] defined for five values of the visual range V_0 equal to 5, 10, 15, 23 and 50 km. The particulate extinction features are represented in terms of i) the maritime aerosol extinction model [19] in model IO, ii) the rural aerosol extinction model [19] in model MS, iii) the urban aerosol extinction model [19] in model US, and iv) the tropospheric aerosol extinction model [19] in model MW. The values of the slope coefficient d found for the four best-fit lines provide the variation in ΔT due to unit increment of $\tau_a(0.55\ \mu\mathrm{m})$.

bimodal maritime aerosol model. All four particle extinction models were defined for relative humidity equal to 50% along the entire vertical atmospheric path [19]. Following the procedure described in sect. **5**, we then calculated the temperature deficit ΔT for all the four sets of atmospheric models obtained inserting into the four atmospheric models MW, MS, US and IO the above aerosol extinction models normalised to five different values of V_0 fixed above. The values of ΔT obtained for all these 20 cases are shown in fig. 13 as a function of $\tau_a(0.55\ \mu\mathrm{m})$, separately for each atmospheric model. The results indicate that ΔT increases almost linearly as a function of aerosol optical thickness $\tau_a(0.55\ \mu\mathrm{m})$, the corresponding best-fit lines yielding values of the slope coefficient d between 0.02 K (tropospheric aerosols) and 1.17 K (maritime aerosols). The different slope coefficients obtained in fig. 13 can be mainly explained in terms of the radiative properties of the columnar aerosols, such as the single scattering albedo and, hence, the scattering and absorption percentages of these columnar aerosol polydispersions, such rates also being strongly influenced by the thermal characteristics of the atmosphere.

In fact, a very low variation of ΔT per unit variation of $\tau_a(0.55\ \mu\mathrm{m})$ was found in the case of model MW, which is the coldest one among those considered in fig. 13. Model MW contains the monomodal tropospheric particle size-distribution having log-normal shape, with mode radius equal to about 0.0275 μm and standard deviation equal to 0.35. This aerosol polydispersion, mainly consisting of small particles, is rather inefficient in producing scattering of infrared radiation, due to the low values of the Mie ratio between

particle sizes and wavelengths. Moreover, it is expected to produce moderate absorption of infrared radiation, the average value of single scattering albedo ω in the 3.5–4.0 μm wavelength range being equal to 0.699, with a monochromatic value of $\omega(3.75\ \mu$m) equal to 0.735 [19].

Higher values of the slope coefficient d, equal to 0.27 and 0.46 K, were obtained for the bimodal models of rural and urban aerosols, associated with models MS and US, respectively, both characterised by temperate thermal conditions. Both polydispersions consist of similar small and large particle modes, the latter causing more important radiative effects in terms of absorption of infrared radiation. In fact, the size-distribution curve consisting of rural aerosols exhibits mode radii equal to about 0.0275 μm and 0.4377 μm and corresponding standard deviations of 0.35 and 0.40, respectively, while the bimodal size-distribution curve of urban particles presents mode radii of about 0.0256 μm and 0.4113 μm and the same values of the standard deviations. In spite of the very similar size-distribution features, the urban aerosols were found to provide more pronounced temperature deficit effects than rural particles, although associated with the colder atmospheric model. Thus, the more marked effects can be reasonably explained by the fact that urban aerosols absorb infrared radiation more efficiently. In fact, the single scattering albedo of the urban aerosol polydispersion assumes an average value of 0.427 in the (3.5–4.0) μm window with a monochromatic value $\omega(3.75\ \mu$m) $= 0.429$ [19], which is considerably lower than that of tropospheric aerosols. The rural particle polydispersion presents an average value of ω equal to 0.899, with $\omega(3.75\ \mu$m) $= 0.914$ [19], which is which is more than twice that of urban aerosols and considerably higher than that attributed to tropospheric aerosols.

A markedly higher value of d, equal to 1.17 K, was determined in the case of the bimodal maritime aerosol model, presumably because of the very warm conditions of the atmosphere represented by model IO, and the presence of an optically predominant fraction of large and giant marine particles, characterised by a wide wing of giant particles. In this case, the bimodal size-distribution curve has mode radii equal to about 0.0275 μm and 0.1711 μm, respectively, and corresponding values of the standard deviation equal to 0.35 and 0.40. The bimodal aerosol polydispersion causes important scattering effects and negligible absorption of infrared radiation, as indicated by parameter ω, which presents an average value equal to 0.975 in the 3.5–4.0 μm window and a monochromatic value $\omega(3.75\ \mu$m) $= 0.982$ [19]. Therefore, the particularly high value of the temperature deficit contribution can be plausibly explained in terms of the very warm conditions of model IO. The upward emission from the surface and the low atmosphere is particularly intense and the upwelling infrared radiation turns out to be attenuated by marine aerosols, being subject to a strong reduction in spite of the kind of radiative effects generated by these almost purely scattering particles.

In order to examine more closely the effects induced by the various columnar aerosol polydispersions on ΔT in the presence of different thermal conditions of the atmosphere, we calculated the values of ΔT for the 23 atmospheric models of table I, representing the columnar aerosol content in terms of the four aerosol extinction models considered above [19], and assuming that $\tau_{\rm a}(0.55\ \mu$m) is equal to 0.235, which corresponds to a visual range $V_0 = 23$ km in all cases. We then calculated the values of ΔT for the 23 atmospheric models in table I, assumed to be without aerosols, that is with $\tau_{\rm a}(0.55\ \mu$m) $= 0$. From these results, we determined for each model the value of the difference $\delta_{\rm a}$ between the value of ΔT calculated for $\tau_{\rm a}(0.55\ \mu$m) $= 0.235$ and the corresponding value of ΔT obtained without aerosols. With this procedure, we defined four sets of differences $\delta_{\rm a}$, corresponding to maritime, rural, urban and tropospheric aerosol polydispersions,
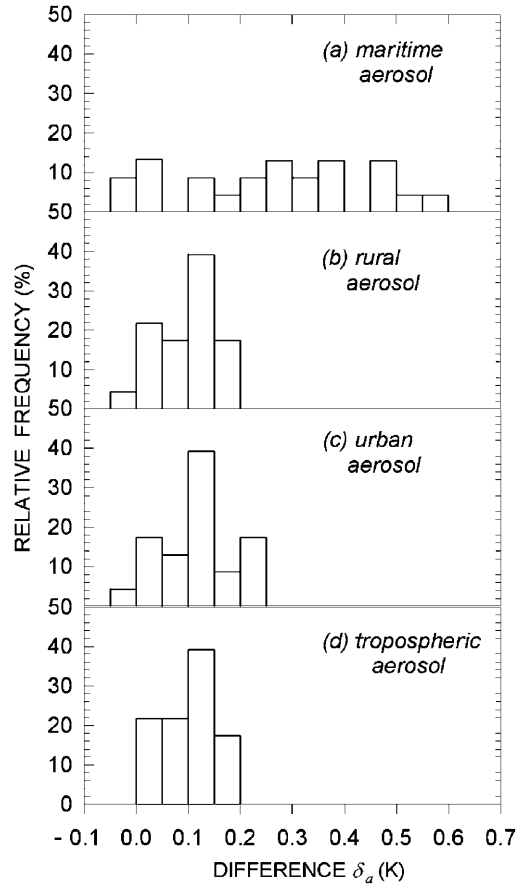
Fig. 14. – Relative frequency histograms of the difference δ_a between the values of temperature deficit ΔT calculated for the 23 atmospheric models listed in table I in the case with aerosol optical thickness $\tau_a(0.55 \ \mu m) = 0.235$ and in the case without aerosols, respectively.

respectively [19]. The relative frequency histograms of δ_a obtained from the four sets relative to different aerosol polydispersions are drawn in fig. 14. The results show that:

a) Maritime aerosols can produce partial contributions of ΔT covering a wide range from -0.05 to 0.60 K, with a median value of 0.28 K and the other two quartiles of 0.12 and 0.38 K, respectively. The results provided an average value of δ_a equal to (0.26 ± 0.18) K, corresponding to a mean value of ΔT per unit $\tau_a(0.55 \ \mu m)$ equal to (1.10 ± 0.80) K, in close agreement with the results found in fig. 13 for model IO.

b) Rural aerosols produce partial values of ΔT ranging from -0.05 to $+0.20$ K, with a median value of 0.11 K and the other two quartiles equal to 0.04 and 0.14 K, respectively. Examining the overall set of values of δ_a, we found an average value of this parameter equal to (0.10 ± 0.06) K and, consequently, a mean value of ΔT per unit $\tau_a(0.55 \ \mu m)$ equal to (0.41 ± 0.25) K.

c) Urban aerosols produce partial values of ΔT varying from -0.05 to $+0.25$ K, with a median value of 0.12 K and the other two quartiles of 0.06 and 0.15 K, respectively.

Correspondingly, we found an average value of δ_a equal to (0.12 ± 0.07) K and a mean value of $\Delta T/\tau_a(0.55~\mu m)$ equal to (0.49 ± 0.31) K.

d) Tropospheric aerosols present a limited range of δ_a, yielding a median value equal to 0.11 K and the other two quartiles of 0.06 and 0.14 K, respectively. Thus, the average value of δ_a was found to be equal to (0.10 ± 0.05) K, giving a mean value of ΔT per unit $\tau_a(0.55~\mu m)$ equal to (0.43 ± 0.22) K.

Therefore, maritime particles turn out to cause the most marked effects on the overall temperature deficit ΔT, which can often exceed 1 K per unit variation of $\tau_a(0.55~\mu m)$. The other evaluations of δ_a determined for rural, urban and tropospheric aerosols were found to vary around a mean value of ratio $\Delta T/\tau_a(0.55~\mu m)$ equal to about 0.45 K, with standard deviations ranging between 0.2 and 0.3 K in all cases. This means that the temperature deficit caused by aerosols within the 3.5–4.0 μm wavelength range can become of comparable intensity with those produced by atmospheric water vapour and those due to the thermal characteristics of the atmosphere only in particular cases of low atmospheric transparency, associated with the presence of considerable loadings of particulate matter in the vertical atmospheric column.

10. – Conclusions

The results obtained in the present analysis indicate very clearly that temperature deficit ΔT closely depends on various parameters. The first is the shape of the vertical profile of temperature, in particular the part including the ground layer, which can be defined by parameters z_j and γ, as shown in fig. 6. Consequently, ΔT appears closely related to the surface temperature T_s, as shown in fig. 7, where precipitable water is assumed to remain constant in all the atmospheric configurations derived from each model. The second one is precipitable water w, producing nearly linear dependence features, with slope coefficients that vary as a function of temperature gradient γ, as shown in fig. 8. Ratio $\Delta T/w$ turns out to decrease as a function of γ, describing the patterns presented in fig. 9, whose slope-coefficients depend strongly on the ground-layer depth where nocturnal cooling or ground heating processes take place. Other two parameters are the atmospheric concentrations of CH_4 and N_2O, which cause dependence features that can be realistically represented in terms of closely linear variations, as in the case shown in fig. 11 for methane, where the slope coefficients vary from one atmospheric model to another, because of their different temperature features. The last parameter identified in the present study is the aerosol optical thickness, which presents nearly linear variations, with slope coefficients depending on the radiative properties of particulate matter and generally decreasing as one passes from warm atmospheres, such as those observed in low-latitude oceanic regions, to cold atmospheres, such as those of mid- and high-latitude areas.

Realistic evaluations of precipitable water and thermal characteristics occurring within the ground layer of the atmosphere can be easily obtained in maritime and land regions, by examining i) the weather synoptic maps prepared by numerous national meteorological services (as part of the WMO activities), as well as simultaneous data-sets provided by networks of ground-based meteorological stations and radiosounding measurements [51-53], and ii) terrestrial surface images taken by various satellite radiometers, within various infrared channels [54-67]. With the help of these data, the results found in the present study can be employed to give form to a procedure aimed at evaluating the temperature deficit ΔT for different seasonal and latitudinal conditions of the atmosphere. The suggested procedure can be divided into the following steps:

1) select a certain area of interest, characterised by cloudless sky conditions, and identify the set of the corresponding pixels to be investigated. Examine the synoptic maps and the other meteorological data-sets and compare them with information derived from the images furnished by NOAA, Meteosat and other satellites, to obtain average estimates of the ground-level temperature T_0 of the atmosphere.

2) Examine the satellite images taken within the water vapour channels, the synoptic maps and the available local radiosounding measurements, to obtain reliable estimates of precipitable water w^* in the same area and within the various pixels.

3) Select the most appropriate atmospheric model among those shown in fig. 10, taking into account the average estimate of T_0 obtained at point 1). It can be used to represent more realistically the atmospheric conditions occurring in that area. For this model, calculate the value of ratio $\Delta T/w$ in terms of eq. (4), where the value of T_0 replaces temperature T_s, and the corresponding best-fit values of coefficients c_0, c_1 and c_2 proposed in table VI are used. In this choice, atmospheric model TR should be taken to represent low-latitude warm atmospheres, the US model mid-latitude temperate atmospheres (during spring and autumn periods), the MW model mid-latitude cold atmospheres in winter months, the MS model mid-latitude warm atmospheres in summer months, the SW model high-latitude cold atmospheres in winter periods, and the SS model mid-latitude warm atmospheres during the summer months.

4) Determine the value of ΔT by multiplying the value of $\Delta T/w$ obtained at point 3) by precipitable water w^* found at point 2).

As shown by the results presented in fig. 10, the value of ΔT determined following the procedure can be mainly attributed to the combined effects produced by water vapour absorption and emission processes, which strongly depend not only on the water vapour mass in the vertical atmospheric column, but also on the thermal conditions of the low atmosphere, where the main part of precipitable water is present. In addition, this estimate of ΔT includes the contributions produced by i) methane for a mean atmospheric concentration $C(CH_4) = 1.72$ p.p.m.; ii) nitrous oxide for a mean atmospheric concentration $C(N_2O) = 0.32$ p.p.m.; and iii) rural aerosol particles with optical thickness $\tau_a(0.55\ \mu m) = 0.235$, which corresponds to the visual range $V_0 = 23$ km. Therefore, in all cases where variations in $C(CH_4)$, $C(N_2O)$ and $\tau_a(0.55\ \mu m)$ should occur within the pixels under investigation, further corrections become necessary in order to obtain the most reliable estimates of ΔT. For this purpose, the following remarks should be taken into account:

a) Temperature deficit increases as $C(CH_4)$ increases with a mean slope of 0.24 K (p.p.m.)$^{-1}$ and slopes varying between 0.11 K (p.p.m.)$^{-1}$ in very cold atmospheres and 0.37 K (p.p.m.)$^{-1}$ in very warm atmospheres. Since $C(CH_4)$ currently varies with latitude and season between about 1.80 p.p.m. and no less than 1.52 p.p.m. [68, 69], parameter ΔT is expected to increase by no more than 0.01 K, as one moves toward the highest northern latitudes, and to decrease by no more than 0.03 K, on reaching the highest southern latitudes. Moreover, considering that $C(CH_4)$ is predicted to vary by no more than 0.02 p.p.m./year during the next decade [48], the correction term of ΔT due to methane should vary correspondingly during the next ten years by no more than ± 0.03 K, even for the worse predictions of latitudinal and seasonal conditions. Therefore, ΔT corrections due to CH_4 concentration changes are estimated to be smaller than the error made in evaluating the overall value of ΔT through the above procedure. Thus, in practice we suggest that the methane correction term can be neglected in all cases.

b) A mean evaluation of 1.1 K (p.p.m.)$^{-1}$ was obtained for the N$_2$O temperature deficit, with an overall range from 0.4 to 1.8 K (p.p.m.)$^{-1}$. The average atmospheric concentration $C(N_2O)$ is predicted to increase by 5×10^{-4} p.p.m. per year in the near future [49, 70]. Consequently, the mean global increase of $C(N_2O)$ will be of about 5×10^{-3} p.p.m. in the next decade. This implies that the partial term of ΔT due to N$_2$O is expected to increase correspondingly by about 0.006 K over the next ten years, with minimum and maximum increments of less than 0.01 K, due to variations in the thermal conditions of the atmosphere. Therefore, the temperature deficit correction for N$_2$O can be totally neglected.

c) The evaluations of ΔT shown in figs. 5 to 10 were obtained for $\tau_a(0.55 \ \mu\text{m}) =$ 0.235, *i.e.* for a visual range of 23 km, due to the rural aerosol bimodal model [19]. All these values of ΔT contain an aerosol extinction contribution varying from 0.04 K in very cold atmospheres to 0.16 K in very warm atmospheres, with an average value of 0.10 K pertinent to temperate mid-latitude atmospheres. Moreover, the relative frequency histograms of parameter δ_a, presented in fig. 14 and determined for $\tau_a(0.55 \ \mu\text{m})$ = 0.235, due to aerosol polydispersions of various origins, show that the aerosol temperature deficit per unit $\tau_a(0.55 \ \mu\text{m})$ varies mostly between 0.3 and 1.9 K in the case of maritime aerosols, 0.2 and 0.7 K for both rural and tropospheric aerosols, and 0.2 and 0.8 K for urban aerosols.

On the basis of these results, we decided that the temperature deficit estimates obtained following the procedure described in the present section and based on the use of eq. (4) need to be corrected for the aerosol extinction effects, as follows.

1) In oceanic remote regions, where maritime aerosol particles are predominantly present and produce values of $\tau_a(0.55 \ \mu\text{m})$ mainly ranging between 0.05 and 0.15, each estimate of ΔT obtained from eq. (4) requires correction for rural aerosol extinction effects by subtracting a term which is expected to be equal to i) 0.04 K, in cold atmospheres at high latitudes, ii) 0.10 K, in temperate atmospheres at mid-latitudes, and iii) 0.16 K in warm atmospheres at low latitudes. Thereupon, corrections for the effects generated by aerosols really present in the atmosphere must be made, by adding values of ΔT that are all reliably estimated to increase as $\tau_a(0.55 \ \mu\text{m})$ increases from 0.05 to 0.15, on the basis of the above evaluations. They indicate that such an additional term of ΔT correspondingly increases i) from 0.02 to 0.05 K, in very cold atmospheres, at polar latitudes, ii) from 0.06 to 0.2 K, in temperate atmospheres at mid-latitudes, and iii) from 0.1 to 0.3 K, in warm atmospheres at low latitudes, according to the results found in the case of the Indian Ocean model.

2) The estimates of ΔT obtained from eq. (4) need to be corrected in continental remote regions, where rural and tropospheric aerosols are present with values of $\tau_a(0.55 \ \mu\text{m})$ mostly ranging between 0.05 and 0.15, by subtracting a term that decreases as $\tau_a(0.55 \ \mu\text{m})$ increases from 0.05 to 0.15, as follows: i) from 0.03 K to about 0.01 K, in very cold atmospheres at polar latitudes, ii) from 0.08 K to about 0.04 K, in temperate atmospheres at mid-latitudes, and iii) from 0.13 K to no less than 0.06 K, in warm atmospheres at low latitudes.

3) The estimates of ΔT obtained from eq. (4) need to be increased in continental areas, where anthropic activities are highly developed, since in these regions the vertical aerosol mass loading consists mainly of urban and rural aerosols, which usually contain important fractions of carbonaceous substances. These aerosols produce values of $\tau_a(0.55 \ \mu\text{m})$ mainly ranging between 0.3 and 0.6. Thus, the corrections of ΔT can be made by adding

terms which correspondingly increase with $\tau_a(0.55\ \mu\mathrm{m})$ i) from 0.01 K to no more than 0.07 K, in cold atmospheres at high latitudes, ii) from no less than 0.02 K to more than 0.19 K, at mid-latitudes, and iii) from no less than 0.01 K to about 0.30 K, in warm atmospheres at low latitudes.

The above corrections of ΔT for the aerosol effects can be more reliably made by taking into account the evaluations of $\tau_a(0.55\ \mu\mathrm{m})$, which can be determined within the same pixels by examining satellite images taken in visible and near-infrared radiometric channels, through appropriate retrieval procedures [71-74]. In this way, the present procedure and the evaluations of ΔT carried out in this study can be correctly used to provide reliable estimates of ΔT within the 3.5–4.0 μm spectral range. The corresponding channels used by the AVHRR radiometers mounted on the NOAA-7 to NOAA-16 satellites exhibit normalised spectral response curves higher than 90% within the 3.6–3.9 μm spectral range, as in the case of NOAA-14 satellite, with central wavelengths varying between 3.70 and 3.77 μm. Conversely, the IR3.9 channel of the SEVIRI instrument mounted on the MSG-1 satellite covers an overall wavelength interval from 3.48 to 4.36 μm, centred at 3.90 μm. Therefore, the present findings are estimated to provide useful evaluations of ΔT for applications to radiance AVHRR measurements. With regard to the SEVIRI radiance measurements, the present results can be utilized to derive reliable evaluations of the intensity of the effects produced within the IR3.9 channel wavelength range by the thermal characteristics of the atmosphere, water vapour, methane, and aerosols. More precise calculations are presumably required for evaluating the N_2O and CO_2 absorption effects.

REFERENCES

[1] TOMASI C. and TROMBETTI F., *Riv. Nuovo Cimento*, **8**, No. 2 (1985).
[2] DAVIS P. A., *Spectral Radiance-Temperature Conversions for Measurements by AVHRR Channels 3, 4, 5.* NOAA Technical Report NESDIS 71, U. S. Department of Commerce, Washington, D. C. (1993).
[3] GOÏTA K., ROYER A. and BUSSIÈRES N., *Remote Sens. Environ.*, **60** (1997) 282.
[4] GOÏTA K. and ROYER A., *IEEE Trans. Geosci. Remote Sens.*, **35** (1997) 718
[5] SCHMETZ J., PILI P., TJEMKES S., JUST D., KERKMANN J., ROTA S. and RATIER A., *Bull. Am. Meteorol. Soc.*, **83** (2002) 977.
[6] SCHMETZ J., PILI P., TJEMKES S., JUST D., KERKMANN J., ROTA S. and RATIER A., *Bull. Am. Meteorol. Soc.*, **83** (2002) ES50.
[7] FAAS H., BUHLER Y. and GÜTTLICH J., *The MSG Application Ground Segment*, in *Proceedings of the 1996 Meteorological Satellite Data Users' Conference*, EUM P19 ISSN 1011-3932, *Vienna (Austria) 16th-20th September 1996*, pp. 23-29.
[8] DESCHAMPS P. Y. and PHULPIN T., *Boundary-Layer Meteorol.*, **18** (1980) 131.
[9] BARTON I. J., *Q. J. R. Meteorol. Soc.*, **109** (1983) 365.
[10] LLEWELLYN-JONES D. T., MINNET P. J., SAUNDERS R. W. and ZAVODY A. M., *Q. J. R. Meteorol. Soc.*, **110** (1984) 613.
[11] STRONG A. E. and McCLAIN P. A., *Bull. Am. Meteorol. Soc.*, **65** (1984) 138.
[12] DESBOIS M., SEZE G. and SZEJWACH G., *J. Appl. Meteorol.*, **21** (1982) 401.
[13] SCHMID J., The SEVIRI instrument, in *Proceedings of the 2000 EUMETSAT Meteorological Satellite Data Users' Conference, Bologna (Italy), 29 May-2 June 2000* (2000), pp. 23-32.
[14] VITTORI O., TOMASI C. and GUZZI R., *J. Atmos. Sci.*, **31** (1974) 261.
[15] KONDRATYEV K. YA., *Radiation in the Atmosphere* (Academic Press, New York) 1969, pp. 85-159.

[16] KNEIZYS F. X., SHETTLE E. P., ABREU L. W., CHETWIND J. H., ANDERSON G. P., GALLERY W. O., SELBY J. E. A. and CLOUGH S. A., *Environmental Research Papers*, No. 1010, AFGL-TR-88-0177, Hanscom AFB, Massachusetts (16 August 1988).

[17] MCCLATCHEY R. A., FENN R. W., SELBY J. E. A., VOLZ F. E. and GARING J. S., *Environmental Research Papers*, No. 411, AFCRL-72-0497, L. G. Hanscom Field, Massachussetts (August 24, 1972).

[18] ANDERSON G. P., CLOUGH S. A., KNEIZYS F. X., CHETWIND J. H. and SHETTLE E. P., *Environmental Research Papers*, No. 954, AFGL-TR-86-0110, Air Force Geophysics Laboratory, L. G. Hanscom Field, Massachussetts (May 15, 1986).

[19] SHETTLE E. P. and FENN R. W., *Environmental Research Papers*, No. 676, AFGL-TR-79-0214, Hanscom AFB, Massachussetts (September 20, 1979).

[20] BERK A., ANDERSON G. P., ACHARYA P. K., CHETWYND J. H., BERNSTEIN L. S., SHETTLE E. P., MATTHEW M. W. and ADLER-GOLDEN S. M., *MODTRAN N4 User's Manual*, Air Force Research Laboratory, AFMC, Hanscom AFB, Massachussetts (June 1, 1999).

[21] ANDERSON G. P., KNEIZYS F. X., CHETWIND J. H., WANG J., HOKE M. L., ROTHMAN L. S., KIMBALL L. M., MCCLATCHEY R. A., SHETTLE E. P., CLOUGH S. A., GALLERY W. O., ABREU L. W., SELBY J. E. A., *FASCODE/ MODTRAN/ LOWTRAN: Past/ Present/ Future*, in *Proceedings of the 18th Annual Review Conference on Atmospheric Transmission Models (6-8 June 1995)*.

[22] BENEDICT W. S., *J. Chem. Phys.*, **24** (1956) 1139.

[23] SPENCER D. J., DENAULT G. C. and TAKIMOTO H. H., *Appl. Opt.*, **13** (1974) 2855.

[24] WHITE K. O., WATKINS W. R., BRUCE C. W., MEREDITH R. E. and SMITH F. G., *Appl. Opt.*, **17** (1978) 2711.

[25] HARRISON A. W., *Boundary-Layer Meteorol.*, **5** (1973) 365.

[26] MCCLATCHEY R. A., BENEDICT W. S., CLOUGH S. A., BURCH D. E., CALFEE R. F., FOX K., ROTHMAN L. S. and GARING J. S., *Environmental Research Papers*, No. 434, AFCRL-TR-75-0096, L. G. Hanscom Field, Massachusetts (January 26, 1973).

[27] ROTHMAN L. S., GOLDMAN A., GILLIS J. R., GAMACHE R. R., PICKETT H. M., POYNTER R. L., HUSSON N. and CHEDIN A., *Appl. Opt.*, **22** (1983) 1616.

[28] ROTHMAN L. S., GAMACHE R. R., BARBE A., GOLDMAN A., GILLIS J. R., BROWN L. R., TOTH R. A., FLAUD J.-M. and CAMY-PEYRET C., *Appl. Opt.*, **22** (1983) 2247.

[29] BURCH D. E. and ALT R. L., *Continuum Absorption by H_2O in the 700-1200 cm^{-1} and 2400-2800 cm^{-1} Windows*, Air Force Geophysics Laboratory Report No. AFGL-TR-84-0128, Hanscom AFB, Massachussetts (1984).

[30] BIGNELL K. J., *Q. J. R. Meteorol. Soc.*, **96** (1970) 390.

[31] KNEIZYS F. X., SHETTLE E. P., GALLERY W. O., CHETWIND J. H. JR., ABREU L. W., SELBY J. E. A., FENN R. W. and MCCLATCHEY R. A., *Environmental Research Papers*, No. 697, AFGL-TR-80-0067, Hanscom AFB, Massachussetts (February 21, 1980).

[32] HÄNEL G., *Adv. Geophys.*, **19** (1976) 73.

[33] TOMASI C. and TAMPIERI F., *Tellus*, **29** (1977) 66.

[34] WHITBY K. T., *Atmos. Environm.*, **12** (1978) 135.

[35] GRASSL H., *Tellus*, **25** (1973) 386.

[36] VOLZ F. E., *Appl. Opt.*, **11** (1972) 755.

[37] VOLZ F. E., *Results on aerosol light absorption*, in *Light Absorption by Aerosol Particles*, edited by H. E. GERBER and E. E. HINDMAN (Spectrum Press, Hampton, Virginia, USA), 1982, pp. 357-372.

[38] TOMASI C., *Pure Appl. Geophys.*, **116** (1978) 1063.

[39] TOMASI C. and PACCAGNELLA T., *Pure Appl. Geophys.*, **127** (1988) 93.

[40] TOMASI C., *J. Geophys. Res.*, **89** (1984) 2563.

[41] TOMASI C. and DESERTI M., *Vertical Distribution Models of Water Vapour for Radiative Transfer Calculations in the Atmosphere*, Technical Paper No. 1, FISBAT-TP-88/1, Bologna (May 5, 1988) (Copies of this paper are available at the Institute ISAC, C. N.R., Bologna (Italy)).

[42] ELTERMAN L., *Environmental Research Papers*, No. 285, AFCRL-68-0153, L. G. Hanscom Field, Massachusetts (April, 1968).

[43] TOMASI C., *J. Appl. Meteorol.*, **21** (1982) 931.

[44] TOMASI C. and VITALE V., *Nuovo Cimento C*, **7** (1984) 35.

[45] TOMASI C., VITALE V. and BENCIVENNI S., *Influence of temperature structure, water vapour, aerosol particles and minor gases on the satellite-borne SST measurements*, in *IRS '92: Current Problems in Atmospheric Radiation*, edited by S. KEEVALLIK and O.KÖRNER (A. Deepak Publ., Hampton, Virginia, USA), 1993, pp. 409-412.

[46] TOMASI C., VITALE V. and BENCIVENNI S., *Calculations of the atmospheric correction terms for surface temperature measurements from Meteosat infrared data*, in *Proceedings of the 9th Meteosat Scientific Users' Meeting*, EUMETSAT, EUM P 11 ISSN 1011-3932, *Locarno (Switzerland), 15th-18th September, 1992*, pp. 369-375.

[47] GRASSL H., *Land surface temperature from satellite data*, in *Agrometeorology*, edited by F. PRODI, F. ROSSI, G. CRISTOFERI (Fondazione Cesena Agricoltura Publ., Cesena, Italy), 1987, pp. 3-26.

[48] STEELE L. P., DLUGOKENCKY E. J., LANG P. M., TANS P. P., MARTIN R. C. and MASARIE K. A., *Nature*, **358** (1992) 313.

[49] KHALIL M. A. K. and RASMUSSEN R. A., *J. Geophys. Res.*, **97** (1992) 14651.

[50] VERMOTE E., TANRÉ D., DEUZÉ J. L., HERMAN M. and MORCRETTE J. J., 1997, *Second Simulation of the Satellite Signal in the Solar Spectrum (6S)*, 6S User Guide Version 2 (Lille, Universitè de Lille, France) 1997, 218 pp.

[51] LALLY V. E., *Upper air in situ observing systems*, in *Handbook of Applied Meteorology*, edited by D. D. HOUGHTON (John Wiley and Sons Inc., New York), 1985, pp. 352-360.

[52] ELLIOTT W. P. and GAFFEN D. J., *Bull. Am. Meteorol. Soc.*, **72** (1991) 1507.

[53] GARAND L., GRASSOTTI C., HALLE J. and KLEIN G. L., *Bull. Am. Meteorol. Soc.*, **73** (1992) 1417.

[54] PRICE J. C., *Remote Sensing Environ.*, **13** (1983) 353.

[55] DALU G., *Int. J. Remote Sens.*, **7** (1986) 1089.

[56] WALTON C. C., *J. Appl. Meteor.*, **27** (1988) 115.

[57] SCHUTT J. B. and HOLBEN B. N., *Proc. IGARSS '91, Helsinki (Finland), June 3-6, 1991*, pp. 1179-1181.

[58] HARRIS A. R. and MASON I. M., *Int. J. Remote Sens.*, **13** (1992) 881.

[59] KEALY P. S. and HOOK S. J., *IEEE Trans. Geosci. Remote Sens.*, **32** (1993) 673.

[60] SCHULZ J., SCHLÜSSEL P. and GRASSL H., *Int. J. Remote Sensing*, **14** (1993) 889.

[61] REYNOLDS R. W. and SMITH T. M., *J. Climate*, **7** (1994) 929.

[62] SCHMETZ J., GEIJO C., MENZEL W. P., STRABALA K., VAN DE BERG L., HOLMLUND K. and TJEMKES S., *Beitr. Phys. Atmosph.*, **68** (1995) 345.

[63] CHABOUREAU J. P., CHÉDIN A. and SCOTT N. A., *J. Geophys. Res.*, **103** (1998) 8743.

[64] NOËL S., BUCHWITZ M., BOVENSMANN H., HOOGEN R. and BURROWS J. P., *Geophys. Res. Lett.*, **26** (1999) 1841.

[65] MAURELLIS A. N., LANG R., VAN DER ZANDE W. J., ABEN I. and UBACHS W., *Geophys. Res. Lett.*, **27** (2000) 903.

[66] EMERY W. J., CASTRO S., WICK G. A., SCHLÜSSEL P. and DONION C., *Bull. Am. Meteorol. Soc.*, **82** (2001) 2773.

[67] ESCOFFIER C., BATES J. J., CHEDIN A., ROSSOW W. B. and SCHMETZ J., *J. Geophys. Res.*, **106** (2001) 5227.

[68] DLUGOKENCKY E. J., MASARIE K. A., LANG P. M., TANS P. P., STEELE L. P. and NISBET E. G., *Geophys. Res. Lett.*, **21** (1994) 45.

[69] DLUGOKENCKY E. J., STEELE L. P., LANG P. M. and MASARIE K. A., *J. Geophys. Res.*, **99** (1994) 17021.

[70] ZANDER R., EHHALT D. H., RINSLAND C. P., SCHMIDT U., MAHIEU E., GUNSON M. P., FARMER C. B., ABRAMS M. C. and KO M. K. W., *J. Geophys. Res.*, **99** (1994) 16745.

[71] IGNATOV A. M., STOWE L. L., SAKERIN S. M. and KORATAEV G. K., *J. Geophys. Res.*, **100** (1995) 5123.

[72] HUSAR R., PROSPERO J. and STOWE L. L., *J. Geophys. Res.*, **102** (1997) 16889.

[73] Nakajima T. and Higurashi A., *Geophys. Res. Lett.*, **25** (1998) 3815.

[74] Durkee P. A., Nielsen K. E., Smith P. J., Russell P. B., Schmid B., Livingston J. M., Holben B. N., Tomasi C., Vitale V., Collins D., Flagan R. C., Seinfeld J. H., Noone K. J., Öström E., Gassø S., Hegg D., Russell L. M., Bates T. S. and Quinn P. K., *Tellus B*, **52** (2000) 484.